

Revised planet brightness temperatures using the Planck/LFI 2018 data release[★]

Michele Maris^{1**}, Erik Romelli¹, Maurizio Tomasi², Anna Gregorio^{3,1}, Maura Sandri⁴, Samuele Galeotta¹, Daniele Tavagnacco¹, Marco Frailis¹, Gianmarco Maggio¹, and Andrea Zacchei¹

¹ INAF/Trieste Astronomical Observatory, Via G.B.Tiepolo 11 - 34143, Trieste, Italy

² Dipartimento di Fisica "Aldo Pontremoli", Università degli Studi di Milano, Via G.Celoria 16, 20133, Milano, Italy

³ Trieste University: Physics Department, Via A. Valerio 2 - 34127, Trieste, Italy

⁴ INAF/Bologna Astronomical Observatory, Via Gobetti 93/3 - 40129, Bologna, Italy

March 2, 2022

ABSTRACT

Aims. We present new estimates of the brightness temperatures of Jupiter, Saturn, Uranus, and Neptune, based on the measurements carried in 2009–2013 by *Planck*/LFI at 30, 44, and 70 GHz and released to the public in 2018. This work extends the results presented in the 2013 and 2015 *Planck*/LFI Calibration Papers, based on the data acquired in 2009–2011.

Methods. *Planck* observed each planet up to eight times during the nominal mission. We processed time-ordered data from the 22 LFI radiometers to derive planet antenna temperatures for each planet and transit. We accounted for the beam shape and radiometer bandpasses, as well as several systematic effects. We compared our results with WMAP's 9th-year results, *Planck*/HFI observations, and existing data and models for planetary microwave emissivity.

Results. For Jupiter, we obtained $T_b = 144.9, 159.8, 170.5$ K (± 0.2 K at 1σ , with temperatures expressed using the Rayleigh-Jeans scale) respectively at 30, 44 and 70 GHz, or equivalently a band averaged Planck temperature $T_b^{(ba)} = 144.7, 160.3, 171.2$ K in good agreement with WMAP and existing models. A slight excess at 30 GHz with respect to models is interpreted as an effect of synchrotron emission. Our measures for Saturn agree with WMAP having for rings $T_b = 9.2 \pm 1.4, 12.6 \pm 2.3, 16.2 \pm 0.8$ K, while for disk we obtained $T_b = 140.0 \pm 1.4, 147.2 \pm 1.2, 150.2 \pm 0.4$ K, or equivalently a $T_b^{(ba)} = 139.7, 147.8, 151.0$ K. Measures for Uranus ($T_b = 152 \pm 6, 145 \pm 3, 132.0 \pm 2$ K, or $T_b^{(ba)} = 152, 145, 133$ K) and Neptune ($T_b = 154 \pm 11, 148 \pm 9, 128 \pm 3$ K, or $T_b^{(ba)} = 154, 149, 128$ K) are well in agreement with WMAP and previous data in literature.

Key words. Cosmology: cosmic background radiation - Planets and satellites: general - Instrumentation: detectors - Methods: data analysis

1. Introduction

The *Planck* mission was led by the European Space Agency (ESA) and measured the intensity and polarization of the microwave radiation from the sky in a wide frequency range (30–850 GHz). The primary scientific purpose of the mission was to fully characterize the spatial anisotropies of the flux of the Cosmic Microwave Background (CMB) over the full sky sphere, as well as to measure the polarization anisotropies of the CMB itself. Secondary science done with *Planck* data has provided important results in several domains of astrophysics, e.g., characterization of Galactic cold clumps, detection of Sunyaev-Zeldovich sources, etc. The *Planck* spacecraft orbited around the L_2 Lagrangian point of the Sun-Earth system and measured the full sky sphere once every six months. The spacecraft hosted two instruments: the High Frequency Instrument (HFI) was an array of bolometers working in the 100–850 GHz range, while the Low Frequency Instrument (LFI) was an array of HEMT-based polarimeters working in the 30–70 GHz range. Because of the design of the 100 mK cooling system used to cool down its bolometers, HFI was able to perform its measurements till January 2012. On the other side, LFI has been operated without significant interruptions for 4 years, completing 8 surveys of the sky.

We present here new estimates for the flux densities of Jupiter, Saturn, Uranus, and Neptune in the frequency range 30–70 GHz, obtained using the Low Frequency Instrument (LFI) onboard the *Planck* spacecraft. This work follows Planck Collaboration (2017), which presented estimates for the same planets using HFI data at higher frequencies (100–850 GHz). *Planck*'s observations have been carried over the period from August 2009 to September 2013. Each planet has been observed 7 or 8 times, and each observation lasted a few days. We have used the data included in the latest *Planck* data release (Planck Collaboration 2018a), which implements the most recent and accurate calibration and systematics removal algorithms, as described in the *Planck* Explanatory Supplement¹.

The importance of planetary measurements for a mission like *Planck* stems from several reasons:

[★] Accepted for the publication December 3, 2020

^{**} Corresponding author e-mail: michele.maris@inaf.it.

¹ https://wiki.cosmos.esa.int/planck-legacy-archive/index.php/Main_Page

1. Planets like Jupiter and Saturn are bright sources when observed at the frequencies used by CMB experiments: the signal-over-noise ratio (S/N) for measurements of the flux of Jupiter using LFI can be greater than 300. Thus, the measurement of their flux can be used as a way to calibrate the instrument or to assess the quality and stability of the calibration. Moreover, it can be used to compare the calibration among different experiments.
2. Planets are nearly point sources when observed with the beams used in typical CMB experiment: the largest apparent radius of a planet is always less than one arcminute, thus smaller than the typical resolution of CMB surveys. This fact, combined with the remarkable brightness of planets like Jupiter and Saturn, permits to calibrate the response of the optical system.
3. Last but not least, one can put constraints on radiative transfer modelling of gaseous planets like Jupiter and Saturn, which are useful to better understand their structure.

We did not use planets to calibrate the LFI detectors in any of the *Planck* data releases (Planck Collaboration 2014d, 2016c). The Doppler effect caused by the motion of the spacecraft with respect to the rest frame of the CMB produces a dipolar signature in the CMB itself that is better suited for the calibration of LFI and HFI. In fact, if compared with Jupiter and other point-like bright sources, the dipole is always visible and its spectrum is identical to the CMB anisotropies. As a consequence, the scanning strategy adopted by *Planck* was not optimized to observe planets and other point sources. Planets were observed whenever beams were close enough to them: this happened roughly twice per year for each of the planets considered in this work, i.e., Jupiter, Saturn, Uranus, and Neptune. In this paper, we do not present results about Mars. Due to its larger proper motion and time variability, the analysis of its observations requires a more complex approach, which we postpone to a future work.

In Planck Collaboration (2014c, 2016b), we used Jupiter’s observations to characterize the beam response of each LFI detector. For the kind of beams used in experiments like Planck, beam responses are characterized by a nearly-Gaussian peak centred along the beam axis, whose Full Width Half Maximum (FWHM) characterizes the angular resolution of the instrument. Far from the beam axis, the beam response is significantly smaller (roughly 0.1–0.4 %), but its characterization is still important because it can lead to non-negligible systematics (Planck Collaboration 2014b, 2016a). Therefore, Planck Collaboration (2014c, 2016b) used numerical simulations to estimate the beam response over the 4π sphere and used Jupiter measurement to validate the simulations within a few degrees from the beam axis, in the regions that are called *main beam* and *intermediate beam* (as explained in Sect. A.1).

The structure of this paper is the following: in Sect. 2 we present a general review of the terms and conventions used in the field, as well as the geometry of observations and a description of the way LFI radiometers measure the signal from the sky. In section 3, we explain how we derived estimates of planet antenna temperatures from the timelines acquired by the LFI radiometers. In particular, section 3.4 contains a description of the method we used to convert antenna temperatures into brightness temperatures, which are physically more significant. Section 4 uses the estimates derived in Sect. 3.4 to compare our estimated SEDs with those produced by the WMAP team. Finally, Sect. 5 sums up the results of this work. The appendix A contains detailed information about our data analysis pipeline.

2. Methodology and models used in the analysis

In this section, we define the frame of reference and conventions that we use in the following sections to describe the observing conditions and the planet signal. When possible, we adhere to the conventions used in Planck Collaboration (2017).

Our approach to the analysis of planetary signals is the following: we model how the Spectral Energy Distribution (SED) of a planet produces a signal, measured as an antenna temperature, and from this result we provide a chi-squared formula to derive the best estimate of the SED using the observations. Having an estimate of the SED, it is then possible to derive an estimate of the brightness of the planet.

2.1. *Planck/LFI focal plane, scanning strategy and observing conditions*

Timing and geometry of planets transits depend on *Planck*’s focal plane geometry, scanning strategy, and orbit. These are fully described in Planck Collaboration (2014a,c). Here we recall that during nominal operations *Planck* scanned the sky spinning at a nearly constant rate of about 1 rotation per minute around its spin axis \hat{S} . The vector \hat{S} was kept stable for some time, equivalent to 30–60 rotations, and then depointed by a small amount. This provides a fundamental time scale for the analysis of *Planck*’s observations, the *pointing period*, which is composed by a short period with unstable spin axis and unreliable attitude reconstruction, followed by a long stable period when attitude information can be derived reliably.

The focal plane of *Planck/LFI* contains 22 beams, which belong to 11 horns. Each beam is sensitive to one of the two orthogonal linear polarizations of each horn, and it feeds a dedicated radiometric chain. The two polarizations are denoted in many ways in *Planck*’s papers: S/M, 1/0, X/Y. For instance: 27-1, 27X and 27S are the same polarized beam in horn 27². Beams in the focal plane aims at fixed positions with respect to \hat{S} and the spacecraft structure, so that each beam scanned the sky in circles with radii defined by their boresight angle β_m : this is the angle between the effective spin axis \hat{S} of the spacecraft and the pointing direction \hat{P} of the beam.

Horns on the focal plane are paired according to the scan direction. Listing the pairs in order of increasing boresight angles we have:

1. LFI18/23, LFI19/22, LFI20/21 (70 GHz);
2. LFI25/26 (44 GHz);
3. LFI24 (44 GHz), LFI27/28 (30 GHz).

² This can be summarized by the so-called “six (S-1-X) rule”.

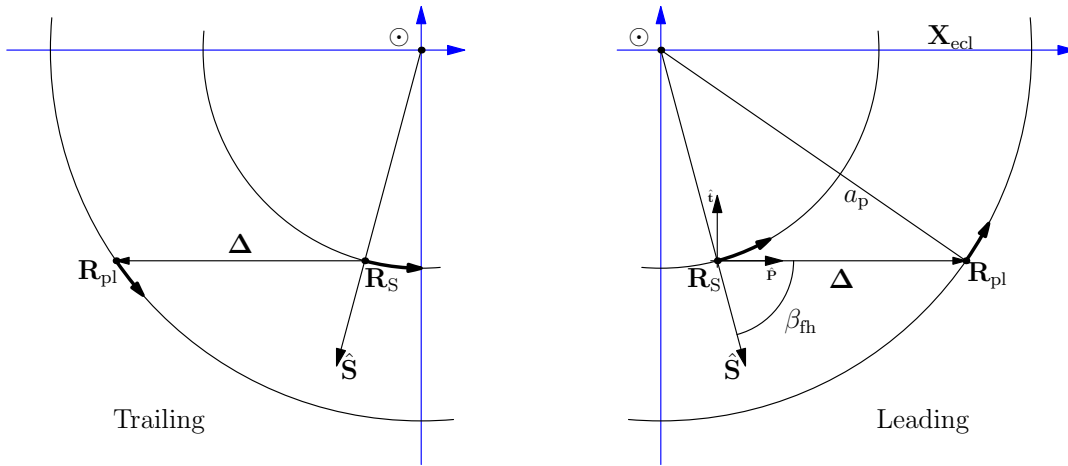


Fig. 1: Geometrical configuration of a planet observation by *Planck*. Left and right frames refer to trailing and leading observations respectively. The position of the spacecraft is marked using \mathbf{R}_S , the position of the planet using \mathbf{R}_{pl} . The Sun is marked with the symbol \odot . Both the spacecraft and the planet revolve counter-clockwise around the Sun in circular and coplanar orbits. For a detailed discussion of the symbols, see the text.

Note that LFI24 (44 GHz) is alone and is nearly aligned with the LFI27/28 pair. Paired horns see a source in the sky nearly at the same time. However, owing to different boresight angles, the same source transits through different pairs at different times. The direction of the orbital motion of the *Planck* spacecraft splits a scan circle into a *leading* and a *trailing* side, the former being the side toward which *Planck* is moving. Transits are classified accordingly. For planets, in leading transits the angle between the planet and the spin axis increases in time, so the planet will be observed at first by LFI18/23 and at last by LFI27/28 plus LFI24. The opposite occurs in the trailing case. However, the geometry of the transits is such that a pair with a larger boresight angle will observe the planet when it will be nearer to the spacecraft than a pair with a smaller boresight angle, irrespectively of the fact that the transit is leading or trailing. Therefore, LFI27/28 and LFI24 will always see a planet with a smaller solid angle than LFI18/23.

The apparent motion of a planet in the reference frame of a beam is complex. The *Planck* team implemented a number of predictors and used them at different stages of mission planning (Maris & Burigana 2009). The principle behind them can be derived from Fig. 1, which shows the most important parameters that describe a transit within a beam: (1) the beam boresight angle β_{fh} , (2) the location of the spacecraft at the epoch of observation within the Solar System \mathbf{R}_S , and (3) the corresponding planet location \mathbf{R}_{pl} . The figure defines the Spacecraft-Planet vector

$$\Delta = \mathbf{R}_{pl} - \mathbf{R}_S, \quad (1)$$

and the instantaneous planet boresight angle β

$$\cos \beta = \hat{\mathbf{S}} \cdot \mathbf{R}_{pl}. \quad (2)$$

Using these quantities, the condition for a transit is

$$|\beta - \beta_{fh}| \leq \text{FWHM}, \quad (3)$$

with FWHM the Full Width Half Maximum (FWHM) of the beam.

Figure 2 is adapted from Planck Collaboration (2016c) and depicts β (continuous line) as a function of observational epoch. Jumps and interruptions in the line denotes changes in the scanning strategy. The gray band in the figure represents the range of β_{fh} angles for the whole set of the *Planck*/LFI feed-horns. It is important to note that LFI27/28 (30 GHz) and LFI24 (44 GHz) have the smallest β_{fh} , LFI25/26 (44 GHz) have the largest β_{fh} , and LFI18–23 (70 GHz) have β_{fh} within these extremes, *Planck*/HFI beams fall in the latter category too. Sometimes transits are indicated either with (L) or (T), whether the planet encounters the scan circle in its leading or trailing sides, defined with respect to the direction of the *Planck* orbital motion. In a (L) transit, the planet enters the scan circle from outside, that is, $\dot{\beta} < 0$, while in a (T) transit the planet exits the scan circle from inside. The labels SS1... SS8 are used to indicate the eight *Planck* sky surveys. In general, planet transits are labelled sequentially as Tr1... Tr8, but there is no one-to-one correspondence between transits and surveys. For example, no Jupiter transits occurred in SS4, but two transits occurred in SS5 (Tr4 and Tr5). In Fig. 2, as in the rest of the paper, we follow the convention of marking epochs in *Planck* Julian Days (PJD), which is the number of Julian Days after the launch; therefore,

$$\text{PJD} = \text{JD} - 2454964.5. \quad (4)$$

In Sect. 4, we tabulate the geometrical quantities described in this section for each planet and transit: see Tables 5 (Jupiter), 8 (Saturn), 11 (Uranus), and 12 (Neptune). The meaning of the columns is the following:

1. “Tr” lists the transit;
2. “Epoch” is the calendar date of the middle of the transit;

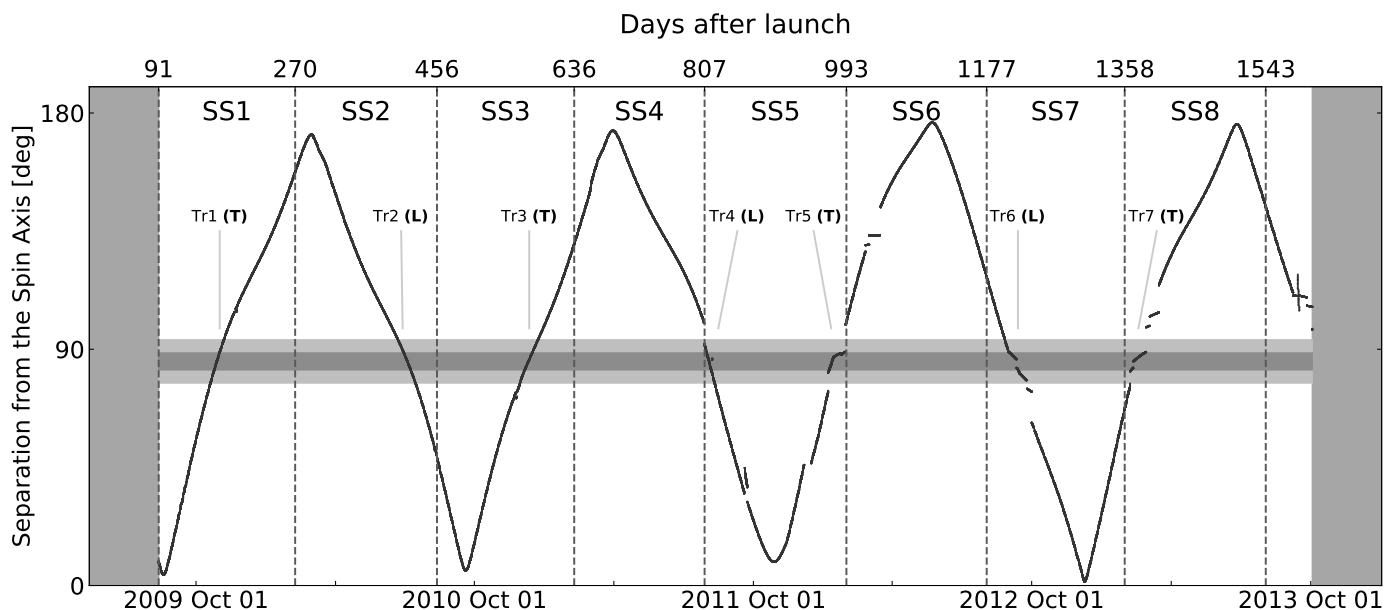


Fig. 2: Time dependence of the angle between Jupiter’s direction and the spin axis of the *Planck* spacecraft. The darker horizontal bar indicates the angular region of the 11 LFI beam axes, while the lighter bar is enlarged by $\pm 5^\circ$. Saturn, Uranus, and Neptune show a similar pattern. The labels SS1...SS8 denote *Planck* sky surveys, as defined in Planck Collaboration (2016c), from which the figure is taken. Tr1...Tr7 denote the transits; letters T and L indicate whether it was a trailing or Leading transit, according to Fig. 1.

3. “PJD” is the start and end epoch, expressed as *Planck* Julian Dates (*begin* refers to the epoch when the planet enters in one of the main beams for the first time, and *end* the last time when it is seen).
4. “Nsmpl” is the number of samples in the timeline that were acquired while the planet was within a main beam;
5. “EcLon” and “EcLat” are the Ecliptic coordinates of the planet as seen from *Planck*;
6. “GalxLat” is the Galactic Latitude of the planet as seen from *Planck*;
7. $|\mathbf{R}_{pl}|$ is the Sun–Planet distance;
8. Δ is the *Planck*–planet distance;
9. Θ_p is the apparent angular diameter of the planet;
10. D_p is the aspect angle of the planet as observed by *Planck* ($0^\circ/90^\circ$ means that the planet is seen along the Equator/Poles), but it represents also the sub-*Planck* latitude observed from the planet at the epoch when the radiation observed by *Planck* left the planet (see Sect. A.5);

All the time dependent quantities are evaluated in the middle of the transit period, which corresponds approximately to the epoch in which the planet transits at the center of the focal plane. These have been computed using the *Horizons* web service³.

2.2. Modelling of planet signals

The power collected by a horn pointing towards some direction $\hat{\mathbf{P}}$ close to a Planet is the sum of four components:

$$\Delta I_{\text{in}} = \Delta I_{\text{in,p}} + \Delta I_{\text{in,bck}} - \Delta I_{\text{in,block}} + \Delta I_0, \quad (5)$$

where $\Delta I_{\text{in,p}}$ is the power delivered by the planet, $\Delta I_{\text{in,bck}}$ the power from the background minus $\Delta I_{\text{in,block}}$ the radiation coming from the background but blocked by the planet, ΔI_0 the noise from the instrument.

The signal from a generic source with spatial brightness distribution $u(\hat{\mathbf{P}})$ (flux over solid angle) and SED $S(\nu)$ is

$$\Delta I_{\text{in}} = \int_0^\infty d\nu \int_{4\pi} d^3\hat{\mathbf{P}}' \tau(\nu) S(\nu) \gamma_\nu(\mathbf{U}_{\text{beam,ecl}}(\hat{\mathbf{P}}, \hat{\Theta}) \cdot \hat{\mathbf{P}}') u(\hat{\mathbf{P}}'), \quad (6)$$

where $\tau(\nu)$ is the instrumental bandpass, $\gamma_\nu(\hat{\mathbf{x}})$ is the pattern of beam response at frequency ν for a pointing direction ($\hat{\mathbf{x}}$) in the beam reference frame, $\mathbf{U}_{\text{beam,ecl}}(\hat{\mathbf{P}}, \hat{\Theta})$ is the matrix describing the transformation from the Ecliptic reference frame to the beam reference frame⁴, accounting for the beam pointing direction $\hat{\mathbf{P}}$ and orientation $\hat{\Theta}$ at the time of observation⁵. Here we assume that $\tau(\nu) \leq 1$, with total bandwidth $\Delta\nu = \int \tau(\nu) d\nu$ and central frequency $\nu_{\text{cent}} = \int \tau(\nu) \nu d\nu / \Delta\nu$. In the following, the dependence on $\hat{\mathbf{P}}$ and $\hat{\Theta}$ will

³ <https://ssd.jpl.nasa.gov/?ephemerides>

⁴ Here and in the following we denote with $\mathbf{U}_{x,y}$ the transformation $y \rightarrow x$, from reference frame y to reference frame x .

⁵ Usually, convolution is denoted as $\int \gamma_\nu(\hat{\mathbf{P}}' - \hat{\mathbf{P}}) u(\hat{\mathbf{P}}') d^3\hat{\mathbf{P}}'$. However, this notation fails to underline that the beam is convolved over the 4π sphere and does not explicitly include $\hat{\Theta}$.

be omitted. If $\hat{\mathbf{e}}_z^{\text{brf}}$ is the versor of the Z axis of the beam reference frame, aligned with the beam optical axis $\hat{\mathbf{P}} = \mathbf{U}_{\text{ecl,beam}} \hat{\mathbf{e}}_z^{\text{brf}}$, then $\gamma_\nu(\hat{\mathbf{e}}_z^{\text{brf}})$ is the peak value of the beam. The quantity

$$\Omega_{\text{beam},\nu} = \frac{\int d^3\hat{\mathbf{P}} \gamma_\nu(\hat{\mathbf{P}})}{\gamma_\nu(\hat{\mathbf{e}}_z^{\text{brf}})} \quad (7)$$

is the beam solid angle at frequency ν . If beam normalization is assumed to have $\int d^3\hat{\mathbf{P}} \gamma_\nu(\hat{\mathbf{P}}) = 1$ then $\gamma_\nu(\hat{\mathbf{e}}_z^{\text{brf}}) = 1/\Omega_{\text{beam},\nu}$. In this paper, we follow the usual convention to map the main beam over a Cartesian (u, v) system drawn on a plane normal to $\hat{\mathbf{e}}_z^{\text{brf}}$ in the beam reference frame, so that pointing $\hat{\mathbf{P}}$ corresponds to the following (u, v) coordinates:

$$\begin{cases} u &= \hat{\mathbf{e}}_x \cdot \mathbf{U}_{\text{beam,ecl}}(\hat{\mathbf{P}}, \hat{\Theta})\hat{\mathbf{P}}; \\ v &= \hat{\mathbf{e}}_y \cdot \mathbf{U}_{\text{beam,ecl}}(\hat{\mathbf{P}}, \hat{\Theta})\hat{\mathbf{P}}. \end{cases} \quad (8)$$

We indicate band-integrated quantities using the apex $^{(\text{ba})}$, like $\Omega_{\text{beam}}^{(\text{ba})}$, $S^{(\text{ba})}$, and so on. Therefore, for a generic source it holds that

$$S^{(\text{ba})} = \frac{1}{\Delta\nu} \int \tau(\nu) S(\nu) d\nu, \quad (9)$$

$$\gamma^{(\text{ba})}(\hat{\mathbf{P}}) = \frac{1}{\Delta\nu S^{(\text{ba})}} \int \tau(\nu) S(\nu) \gamma_\nu(\hat{\mathbf{P}}) d\nu, \quad (10)$$

$$\Omega_{\text{beam}}^{(\text{ba})} = \frac{1}{\gamma^{(\text{ba})}(\hat{\mathbf{e}}_z^{\text{brf}})}. \quad (11)$$

2.3. Estimation of planet signals

We tackle now the problem of connecting the quantities in Eq. (5) to the SEDs of the planets, background, and blocking radiation. For this purpose, we now detail the model behind each of the terms in that equation. Using the conventions presented in the previous paragraphs, the integrated power for planet, background and blocking terms are

$$\Delta I_{\text{in,p}} = \frac{\Omega_{\text{p}}}{\Omega_{\text{beam,p}}^{(\text{ba})}} B_\nu^{(\text{ba})}(T_{\text{b}}^{(\text{ba})}) \Delta\nu g_{\text{p},t}^{(\text{ba})}, \quad (12)$$

$$\Delta I_{\text{in,bck}} = S_{\text{bck}}^{(\text{ba})} \Delta\nu, \quad (13)$$

$$\Delta I_{\text{in,block}} = \frac{\Omega_{\text{p}}}{\Omega_{\text{beam,cmb}}^{(\text{ba})}} B_\nu^{(\text{ba})}(T_{\text{cmb}}) \Delta\nu g_{\text{cmb},t}^{(\text{ba})}, \quad (14)$$

where $B_\nu^{(\text{ba})}(\nu)$ is the band averaged blackbody brightness, it is assumed that the planet is an extended source with solid angle $\Omega_{\text{p}} = \int d^3\hat{\mathbf{P}} u(\hat{\mathbf{P}}) \ll \Omega_{\text{beam}}$, and that most of the blocked radiation is the CMB with SED $B_\nu(T_{\text{cmb}}, \nu)$, so that

$$B_\nu^{(\text{ba})}(T_{\text{cmb}}) = \frac{1}{\Delta\nu} \int_0^\infty d\nu \tau(\nu) B_\nu(T_{\text{cmb}}, \nu). \quad (15)$$

In the equations above, we used the following definition:

$$g_t^{(\text{ba})} = \gamma^{(\text{ba})}(\mathbf{U}_{\text{beam,ecl},t} \cdot \hat{\mathbf{\Delta}}_t), \quad (16)$$

which denotes the band-averaged beam response for a planet located within the main beam at epoch t . This stems from the fact that $\mathbf{U}_{\text{beam,ecl},t} \hat{\mathbf{\Delta}}_t$ is the position of the planet with respect to the beam reference frame, where $\hat{\mathbf{\Delta}}_t$ is the direction in which the planet is seen at time t in the ecliptical reference frame centered on the Spacecraft.

The difference between $g_{\text{p},t}^{(\text{ba})}$ and $g_{\text{cmb},t}^{(\text{ba})}$ is in the SED used to compute the band-averaged integral. Usually, $g_t^{(\text{ba})}$ and $\Omega_{\text{beam}}^{(\text{ba})}$ are averaged accounting for the background SED, but in the following sections we will neglect this detail.

2.4. Converting signals to antenna temperatures

We provide now the equations we used to connect SEDs to antenna temperatures, which are the quantities that are actually measured by the instrument.

Calibration of radiometers maps the measured input power ΔI_{in} onto a scale of antenna temperature variations based on the cosmological dipole, whose antenna temperature ΔT_{dip} depends on the pointing direction $\hat{\mathbf{P}}$ (Planck Collaboration 2014d, 2016c). If we assume that the gain is linear, applying Eq. (6) to the cosmological dipole

$$\Delta I_{\text{dip}}(\hat{\mathbf{P}}) = \left(\frac{dB_\nu}{dT} \right)_{\text{cmb}}^{(\text{ba})} \Delta T_{\text{dip}}(\hat{\mathbf{P}}) \Delta\nu, \quad (17)$$

where ΔT_{dip} is the temperature fluctuation of the cosmological dipole, convolved with the appropriate band-averaged beam pattern

$$\left(\frac{dB_\nu}{dT}\right)_{\text{cmb}}^{(\text{ba})} = \frac{1}{\Delta\nu} \int d\nu \tau(\nu) \left(\frac{dB_\nu}{dT}\right)_{\text{cmb}}(\nu), \quad (18)$$

$$\gamma_{\text{dip}}^{(\text{ba})}(\hat{\mathbf{P}}) = \frac{1}{\left(\frac{dB_\nu}{dT}\right)_{\text{cmb}}^{(\text{ba})} \Delta\nu} \int d\nu \tau(\nu) \left(\frac{dB_\nu}{dT}\right)_{\text{cmb}}(\nu) \gamma_\nu(\hat{\mathbf{P}}) \quad (19)$$

$$\Omega_{\text{beam,dip}}^{(\text{ba})} = \frac{1}{\gamma_{\text{dip}}^{(\text{ba})}(\hat{\mathbf{e}}_z)}. \quad (20)$$

Therefore, the planet signal is mapped onto an equivalent variation of thermodynamic temperature through $\Delta T_{\text{ant,p}}/\Delta T_{\text{dip}} = \Delta I_{\text{in,p}}/\Delta I_{\text{dip}}$. Assuming that the planet is aligned with the center of the beam, the variation of antenna temperature caused by the presence of the planet is

$$\Delta T_{\text{ant,p}}^* = \frac{\Omega_{\text{p}} B_\nu^{(\text{ba})}(T_{\text{b}}^{(\text{ba})})}{\Omega_{\text{beam,p}}^{(\text{ba})} \left(\frac{dB_\nu}{dT}\right)_{\text{cmb}}^{(\text{ba})}}. \quad (21)$$

During a transit, the planet motion within the beam causes a time modulation of the antenna temperature $\Delta T_{\text{ant,t}} \propto g_t^{(\text{ba})} \Delta T_{\text{ant,p}}^*$. Therefore, the planet antenna temperature $\Delta T_{\text{ant,p}}^*$ for each transit and radiometer can be estimated through the minimization of the quantity

$$\chi^2 = \sum_t \frac{1}{\sigma_t^2} \left(\Delta T_{\text{ant,p}}^* g_{\text{p,t}}^{(\text{ba})} + b_t^{\text{m}} - \Delta T_{\text{ant,t}} \right)^2, \quad (22)$$

where σ_t is the confusion noise for the sample at time t , b_t^{m} the background model discussed in Sect. A.2, and $g_t^{(\text{ba})}$ the beam model described in Sect. A.3 and Sect. A.4. A rigorous treatment would include also a term to account for the blocked radiation

$$\Delta T_{\text{ant,block}} = \frac{\Omega_{\text{p}} B_\nu^{(\text{ba})}(T_{\text{cmb}})}{\Omega_{\text{beam,cmb}}^{(\text{ba})} \left(\frac{dB_\nu}{dT}\right)_{\text{cmb}}^{(\text{ba})}}, \quad (23)$$

by the addition of a term $-\Delta T_{\text{ant,block}} g_{\text{cmb,t}}^{(\text{ba})}$ in Eq. (22), as shown in Sect. A.9. This would lead to an estimate for $\Delta T_{\text{ant,p}}^*$ that is already corrected for the blocking factor. However, since blocking is a minor effect, it is customary to correct it later. We chose to follow this approach, and therefore in this work $\Delta T_{\text{ant,p}}^*$ does not include correction for blocking. This convention introduces a small systematic effect, since $g_{\text{p,t}}^{(\text{ba})} \neq g_{\text{cmb,t}}^{(\text{ba})}$. Table 1 summarizes all the radiometer-dependent quantities that are relevant for photometric analysis, which we presented in this section, together with other parameters that will be discussed later.

3. Data Analysis

In this section, we describe the data analysis procedures used to implement the equations presented in Sect. 2. The results of our analysis will be discussed in Sect. 4. Since it is not possible to list the full set of measurements per planet, transit and radiometer inside the paper, we present here only summary plots showing data at different data reduction steps. The technical details of our data analysis pipeline are explained in Appendix A.

3.1. Characteristics of the input data

In our analysis, we have used the Planck 2018 data release, whose timelines have been calibrated using the procedure described in Planck Collaboration (2018b). We do not detail the procedure used to produce these data, but we want to underline a few important details in the Planck/LFI 2018 data processing pipeline:

- The timelines are cleaned of the dipole signal;
- The Galactic pick-up through beam sidelobes has been removed;
- ADC non-linearities have been corrected;
- Pointing has been corrected for a number of systematics⁶.

Each sample in the LFI timelines consists of several fields:

1. UTC time of acquisition;
2. Antenna temperature T_{ant} , calibrated in K_{cmb} ;
3. Apparent pointing direction $\hat{\mathbf{P}}_t$ (direction of the beam axis) in the J2000 reference frame;
4. Beam orientation in the sky;

⁶ https://wiki.cosmos.esa.int/planckpla2015/index.php/Detector_pointing

Table 1: Photometric parameters for *Planck*/LFI radiometers and band averaged beams.

Radiometer ^a	ν_{cent}^b [GHz]	$\Delta\nu$ [GHz]	$B_{\nu,\text{cmb}}^{\text{ba}}$ [MJy/sr]	$\left(\frac{dB_{\nu}}{dT}\right)_{\text{cmb}}^{(\text{ba})}$ [MJy/sr/K]	$B_{\nu,\text{rj},1}$ [MJy/sr/K]	$B_{\nu,\text{rj},1}^{\text{ba}}$ [MJy/sr/K]	$\Omega_{\text{beam}}^{(\text{ba})}$ ^c [$\times 10^5$ sr]	f_{aper} [$\times 10^3$]	f_{η} [$\times 10^3$]	$F_{\text{sync},1}^{(\text{ba})}$ ^d
70-18M	71.738	7.945	214.15	139.05	158.114	159.220	1.673	8.236	3.386	0.693
70-18S	70.096	9.775	208.01	133.64	150.959	152.245	1.703	5.624	2.779	0.699
70-19M	67.513	8.865	198.49	124.95	140.041	140.790	1.625	8.023	3.035	0.709
70-19S	69.695	7.316	206.69	132.15	149.237	150.048	1.610	9.004	4.013	0.700
70-20M	69.174	8.194	204.73	130.43	147.013	147.837	1.549	9.527	3.209	0.703
70-20S	69.585	8.611	206.25	131.82	148.767	149.668	1.553	9.090	3.559	0.701
70-21M	70.412	8.879	209.29	134.60	152.325	153.337	1.537	9.538	3.163	0.698
70-21S	69.696	11.674	206.63	132.20	149.244	150.201	1.559	8.317	3.221	0.701
70-22M	71.483	9.500	213.30	138.14	156.994	157.908	1.586	6.779	2.423	0.693
70-22S	72.788	8.732	218.07	142.56	162.777	163.794	1.605	6.417	2.831	0.689
70-23M	70.764	6.717	210.74	135.63	153.852	154.481	1.679	6.271	2.623	0.696
70-23S	71.322	6.874	212.77	137.55	156.288	157.049	1.693	5.554	2.786	0.694
44-24M	44.451	3.098	109.13	57.84	60.708	60.907	5.080	2.108	0.841	0.838
44-24S	44.060	3.068	107.65	56.91	59.643	59.876	4.961	2.202	0.977	0.841
44-25M	43.995	3.051	107.40	56.72	59.469	59.665	8.250	1.362	1.671	0.841
44-25S	44.184	3.146	108.11	57.17	59.979	60.161	8.723	1.566	1.481	0.840
44-26M	43.949	2.529	107.24	56.65	59.344	59.599	8.276	1.295	1.610	0.842
44-26S	44.074	2.582	107.68	56.89	59.682	59.845	8.699	1.646	1.568	0.841
30-27M	28.345	2.594	52.00	24.29	24.685	24.809	10.011	8.795	2.381	1.004
30-27S	28.536	2.970	52.67	24.66	25.018	25.200	10.074	7.794	2.276	1.002
30-28M	28.790	2.465	53.44	25.06	25.466	25.616	10.050	9.545	2.522	0.998
30-28S	28.155	3.184	51.47	24.03	24.355	24.541	10.068	7.476	2.268	1.007

^a Radiometers are identified by their frequency channel, either 30, 44 or 70 GHz, the feedhorn number, between 18–28, and the polarization arm, either S or M.

^b Central frequency.

^c The radiometric quantities $\Omega_{\text{beam}}^{(\text{ba})}$, f_{aper} and f_{η} refer to a u^2 SED.

^d Band average of the synchrotron spectral dependence $\nu^{-0.4}$ (see Eq. 30) for the 30 and 40 GHz channels.

5. Quality flags;

6. Absolute address of the sample within the global mission timeline.

The pointing directions and beam orientations can be used to compute the $\mathbf{U}_{\text{beam,ecl},t}$ matrix for the sample.

To produce sky maps from timelines, the *Planck*/LFI pipeline needs to reduce the level of noise in the timelines. *Planck*/LFI timelines suffer from the presence of correlated noise, whose spectral shape can be approximated by the function

$$P(f) = \left[1 + \left(\frac{f_k}{f} \right)^\alpha \right] \frac{\sigma^2}{f_s}, \quad (24)$$

where f is the frequency, f_s is the sampling frequency of the detector, σ is the level of white noise in the data, and f_k is the so-called *knee frequency* of the $1/f$ noise; in the case of the *Planck*/LFI receivers, $f_k \approx 20 \div 60$ mHz (Mennella et al. 2010). The presence of $1/f$ noise invalidates many assumptions used in common data-analysis tasks, and several works have dealt with the problem of removing it from time streams. One of the most simple yet effective solutions is the *destriping algorithm*, which is able to determine the time dependence of $1/f$ noise through an approximation of the noise time stream with a number of simple basis functions (Maino et al. 2002; Keihänen et al. 2004). Each basis function is constrained by the requirement that each pass on the same pixel should yield the same measurement, had the noise part in Eq. (24) be negligible. In its simplest incarnation, a destriper uses constant-valued basis functions: in this case, each function is called a *baseline*, and its duration in time must be smaller than $1/f_k$ in order for the destriper to be effective.

Madam (Keihänen et al. 2004), the map-maker implemented in the *Planck*/LFI pipeline, uses a destriping technique to produce frequency maps that are cleaned from correlated noise and a set of baselines that approximate the correlated noise in the timeline. However, we were not able to use this information to clean the timelines in our analysis. One of the fundamental assumptions of the destriping algorithm is that the signal measured on the sky must be constant in time. Therefore, the LFI pipeline masks all those samples acquired while a moving object was within the main beam, and these samples are not considered in the application of the destriping algorithm. We must add that the destriping technique is able to find a reliable solution if there are enough crossings of the same point in the sky among different scan circles. We attempted to use destriping on each planet transit within the main beam of each radiometer: as one transit lasts only a few hours, planets can be considered as fixed point sources. However, the quality of the solution was poor because the number of rings was not enough to fully constrain the solution. A comparison of the estimates for $\Delta T_{\text{ant,p}}^*$ obtained with and without the application of destriping show differences within the random errors due to white noise. For this reason, we decided not to use destriping in our pipeline.

Jupiter, transit=1, fh.arm=27-0, Stokes smeared, pwr+02, BckScale=1.076, BckOffset=2.57e-07

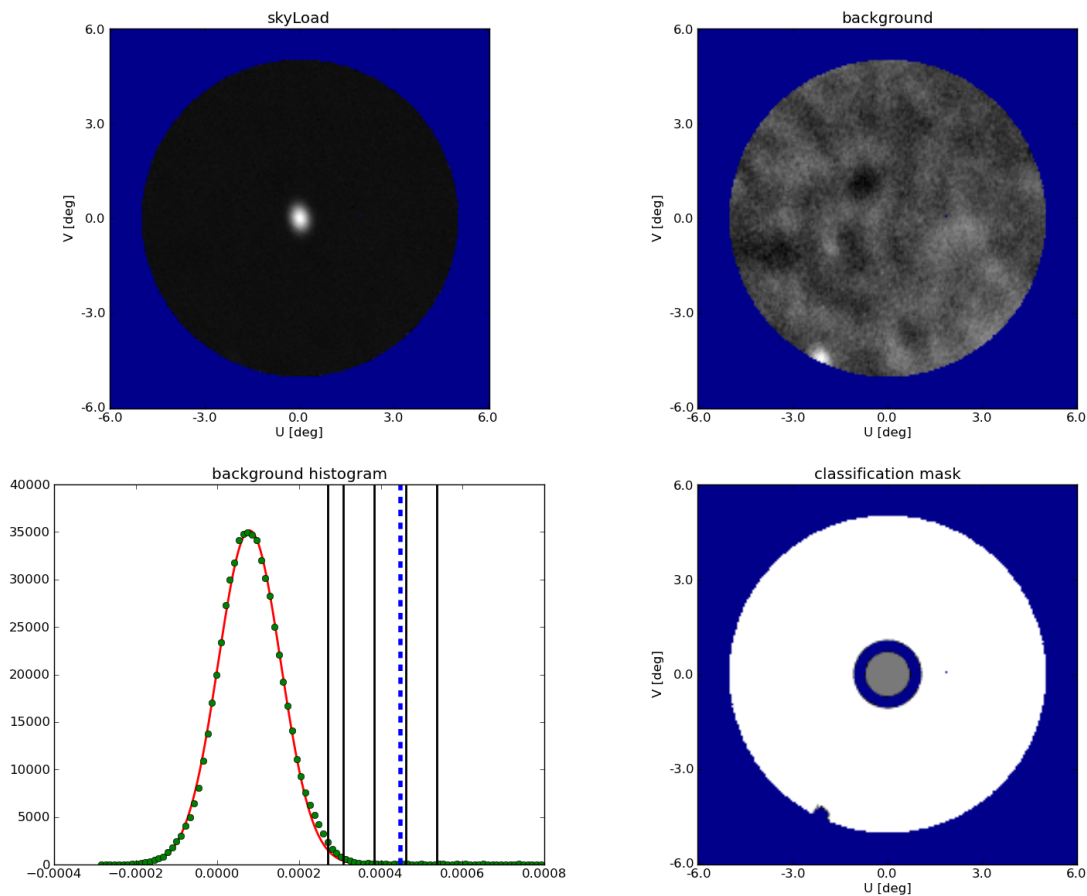


Fig. 3: Example of a map in the (u, v) reference frame for Jupiter. This image shows the first transit as seen by radiometer 27-0 (30 GHz). **Top-left:** map of T_{ant} in K_{cmb} ranging from $-4 \times 10^{-4} K_{\text{cmb}}$ to $0.4 K_{\text{cmb}}$. **Top-right:** map of the background model, expressed as T_{ant} in K_{cmb} ranging from $-4 \times 10^{-4} K_{\text{cmb}}$ to $1 \times 10^{-3} K_{\text{cmb}}$. **Bottom-left:** histogram of T_{ant} in K_{cmb} for the background. The green points mark the samples in the histogram, and the red line is the best-fit Gaussian distribution; the threshold for the classification mask is shown by the dashed blue. **Bottom-right:** classification mask. The gray region shows the planet ROI, the white annulus is the background ROI, and the blue regions mark unused samples.

3.2. Overview of the analysis procedure

To estimate the antenna temperature $\Delta T_{\text{ant,p}}^*$ for the sources considered in this work, we have minimized the value of χ^2 shown in Eq. (22). We only considered those samples that were acquired when the point source fell within a circular region of interest (ROI) centered on the main axis of the beam (details are provided in Sect. A.1), whose radius is always 5° , regardless of the radiometer, transit, or planet. An example of ROI is shown in Fig. 3, top-left frame. As in Planck Collaboration (2014d, 2016c), the background has been estimated by splitting the ROI in two concentric circles: the *planet ROI* and the *background ROI* (see Fig. 3 and Sect. A.1). However, unlike Planck Collaboration (2014d, 2016c), we have not considered the background as a constant but we allow for spatial variations of the background, as described in Sect. A.2. This permits to remove weak background sources and to mask bright sources, as we show in Fig. 3. We model the beam $g_t^{(\text{ba})}$ using a band-averaged map of the main beam, described in Sect. A.3. We account for the apparent motion of the planet and the background within the beam during the acquisition of a sample using the so-called *smearing* algorithm, described in Sect. A.4.

Figure 4 shows the regression of $\Delta T_{\text{ant,p}}^*$ for Jupiter, Saturn, Uranus and Neptune for the first transit and for the three radiometers LFI27-0, LFI24-0, and LFI18-0, which are representative of the 30 GHz, 44 GHz, and 70 GHz frequency channels, respectively. Samples are plotted as a function of the radial distance between the planet and the beam center. Blue and green points represent samples in the planet and background ROIs, while gray points represent samples not used in the fit; the best fit model is represented by red points. The dispersion of red points as a function of radial distance is mainly caused by the ellipticity of the beam. This did not occur for WMAP, as the WMAP team used a symmetrized beam (Weiland et al. 2011; Bennett et al. 2013). Note that there is an apparent increase in dispersion for large radius. This is not due to an actual increase in the variance of the samples, but to the fact that

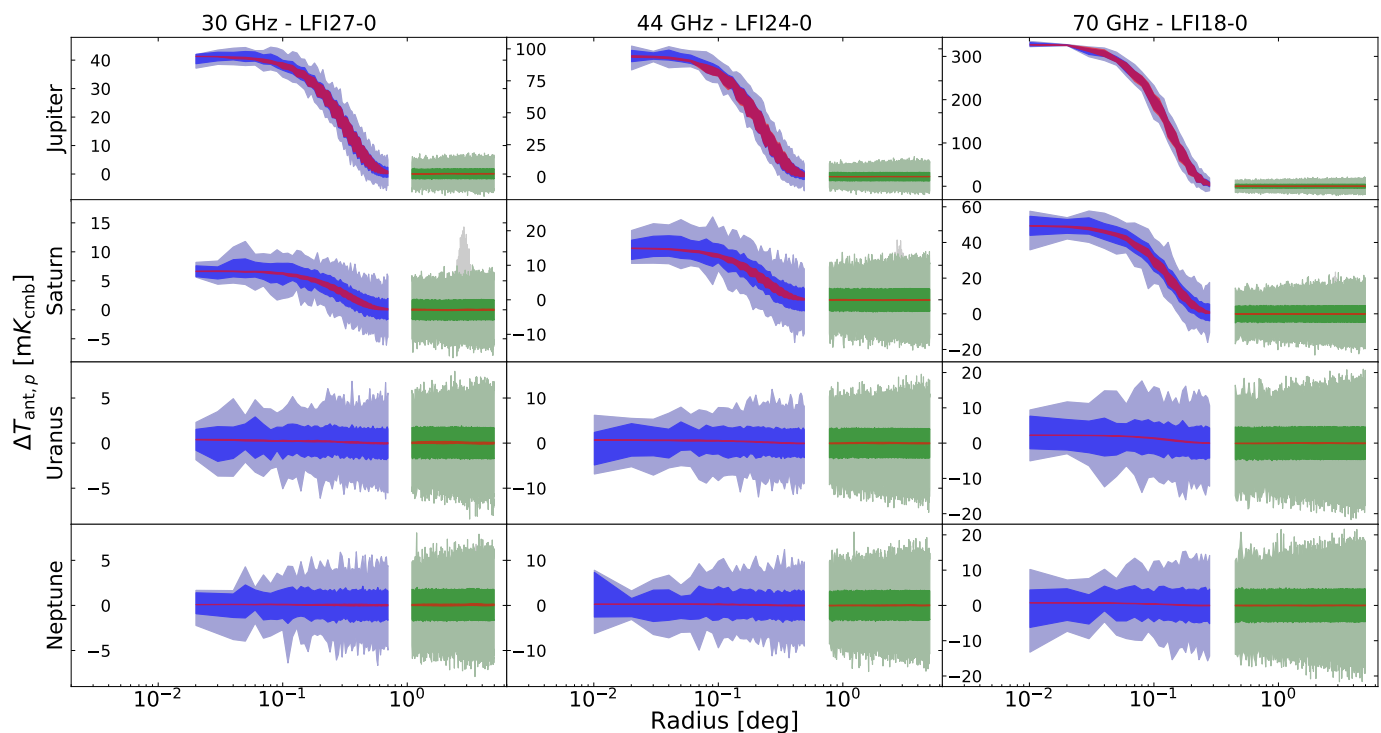


Fig. 4: Antenna temperature estimates T_{ant} for Jupiter, Saturn, Uranus and Neptune (top to bottom) and for three radiometers representative of the 30 GHz (left), 44 GHz (center), and 70 GHz (right) channels, as a function of the angular distance from the beam center. Blue bands shows the distribution of samples in the planet ROI (dark blue: 1σ region, light blue: peak-to-peak variation). Green bands have the same interpretation, but it marks the background ROI. Grey bands show the data before having been σ -clipped; note for the case of Saturn observed by LFI27-0 the presence of a point source, which has been removed before the analysis (not present in the green line). The separation between the blue and green lines marks the presence of the avoidance ROI, not included in our fits. The red line shows the best fit model, and its width is the RMS of the model, due to the ellipticity of the beam.

Table 2: Error bars for $\Delta T_{\text{ant,p}}$.

Planet	30 GHz ^a	44 GHz ^a	70 GHz ^a
Jupiter	15 – 59	37 – 120	75 – 280
Saturn	26 – 62	52 – 120	150 – 300
Uranus	40 – 68	63 – 130	160 – 360
Neptune	42 – 61	62 – 120	170 – 300

^a Values in μK_{cmb} .

at larger distances the population of samples increases in size, thus widening the spanning of the plotted points. LFI data for Jupiter and Saturn show a S/N ratio high enough to be seen in raw data. The same does not hold for Uranus and Neptune.

Figure 5 shows the distribution of the residuals of the fit, radially-averaged in constant-width bins; the bars denote the r.m.s. of the residuals in each bin. In most cases, the radial pattern of the residuals is nearly flat, apart from Jupiter 24 and 27, which show a systematic error with a peak-to-peak amplitude $\lesssim 10^{-3} \text{K}_{\text{cmb}}$ (to be compared with a temperature of $\approx 0.3 \text{K}_{\text{cmb}}$). We chose to neglect this residual, as at this stage it is not easy to understand whether this effect is due to uncertainties in the beam model or bandpass, or to other perturbations. Moreover, the definition of a new beam model for *Planck*/LFI is outside the purpose of this paper.

Figure 6 provides a summary of our measures for $\Delta T_{\text{ant,p}}^*$ for the whole set of planets, transits and radiometers. For Jupiter, and Saturn, the dispersion of $\Delta T_{\text{ant,p}}^*$ is only partially affected by random noise, which introduces a RMS scatter in $\Delta T_{\text{ant,p}}^*$ of at most a few $10^{-4} \text{K}_{\text{cmb}}$. When converted into a relative error per planet, transit and radiometer, the order of magnitude for Jupiter is 10^{-3} , for Saturn 10^{-2} , about 5×10^{-1} for Uranus, and up to 1 for Neptune. The range of errors for our estimates are provided in Table 2.

Because of the small S/N ratio, in some cases the signal for Uranus and Neptune is consistent with zero. This occurs when the confusion noise from the instrument and the background are larger than the signal induced by the planet. Whenever this happened, we removed the affected data from our analysis.

3.3. Estimation of a fiducial antenna temperature

Figure 6 shows some variability among transits and radiometers for the same planet, with a clear pattern in the variation of $\Delta T_{\text{ant,p}}^*$ within the same frequency channel and transit. As an example, $\Delta T_{\text{ant,p}}^*$ for LFI20/21 is larger than for LFI19/22, which in turn is

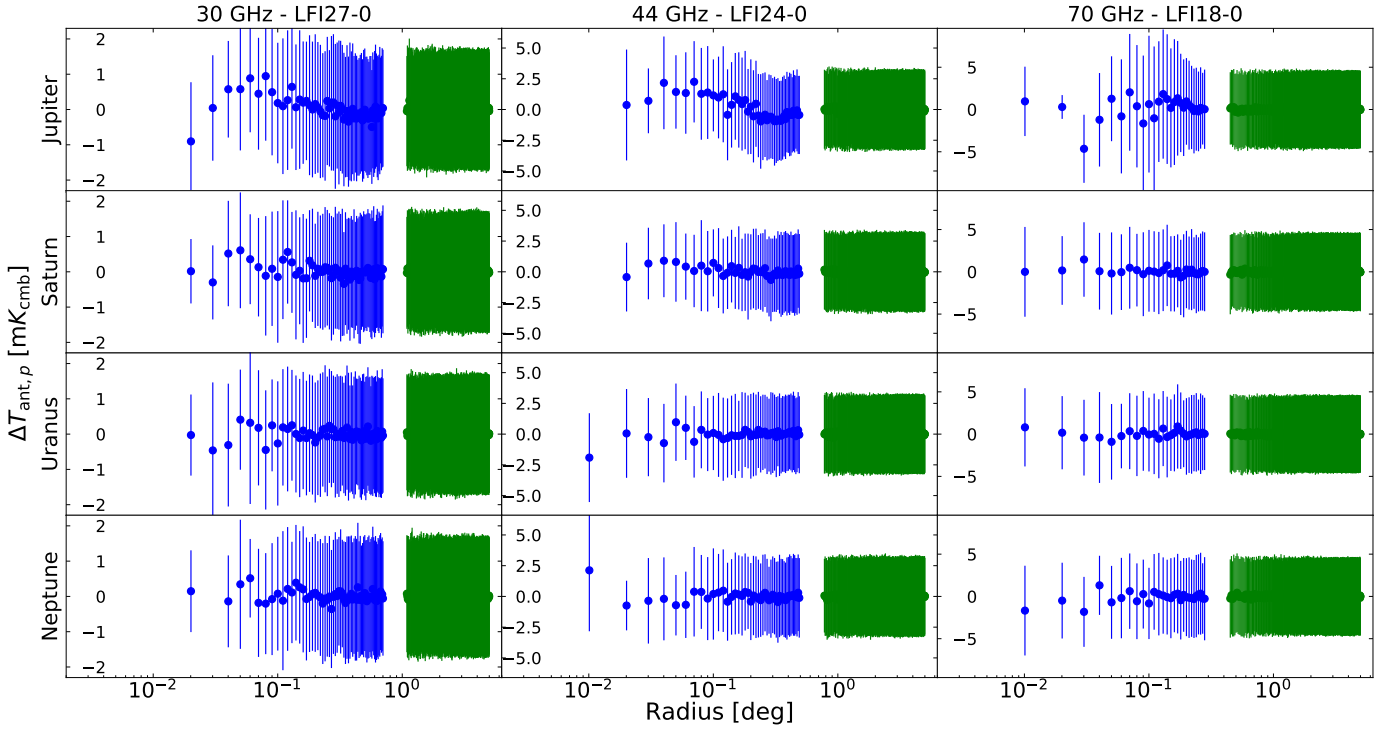


Fig. 5: Radial pattern of residuals averaged over the whole set of transits.

Table 3: Fiducial geometric parameters.

Planet	R_{eq}^a [km]	R_{pol}^b [km]	$\hat{\Delta}^c$ [AU]	$\hat{\Omega}_p^d$ [sterad]
Jupiter	71492	66854	5.2	2.481×10^{-8}
Saturn	60268	54364	9.5	5.096×10^{-9}
Uranus	25559	24973	19.0	2.482×10^{-10}
Neptune	24764	24341	29.0	1.006×10^{-10}

^a Equatorial radius of the planet.

^b Polar radius of the planet

^c Fiducial distance of the planet.

^d Solid angle subtended by the planet.

larger than for LFI18/23. The first reason for these discrepancies is the difference in the value of Ω_{beam} among different radiometers, as this value is largest for the radiometers located far from the center of the focal plane, and producing the bent pattern of the 70 GHz channel or the jump between the horn 24 and the 25 and 26. Secondly, we must consider changes in the circumstances of the observation among different radiometers and transits, which leads to differences in the *Planck*–planet distance $|\Delta|$ (Eq. 1), and so in Ω_p , producing the relative shift of the measurements between one transit and the other. We have considered the change in $|\Delta|$ among different transits, as well as the change occurring while observing the same transit from different horns (refer to Sect. 2.1). Since planets are not spherical, and their polar axis are tilted on their orbital planes, varying observing conditions lead to different apparent aspect ratios of the planets’ shape. In addition we have to take care of systematics of the beam model as its numerical efficiency and the beam aperture. We can reduce antenna temperature to standardized conditions, using the following formula:

$$\widetilde{\Delta T}_{\text{ant,p}} = \frac{\Omega_{\text{beam}}^{(\text{ba})} / \tilde{\Omega}_{\text{beam}} (1 + f_{\text{aper}})(1 + x_{\eta})}{\Omega_p / \tilde{\Omega}_p} \Delta T_{\text{ant,p}}^*, \quad (25)$$

where tilted quantities indicate fiducial values. The meanings of the terms in the equation are the following:

- For each channel we take as a fiducial value $\tilde{\Omega}_{\text{beam}}$, the median of the $\Omega_{\text{beam}}^{(\text{ba})}$ for that channel from Table 1. The actual values we used are: 1.006×10^{-4} sterad (30 GHz), 8.263×10^{-5} sterad (44 GHz), and 1.607×10^{-5} sterad (70 GHz). Since the planet solid angle Ω_p depends on the observer-to-planet distance, $|\Delta|$ (Eq. 1), the reduction to a fiducial solid angle is equivalent to reduction to a fiducial distance. In Table 3, we list the values we used for planet radii, distances to the observer, and solid angles of the planets. Several conventions and approximations are used in the literature to measure distances and solid angles: as an example, distances to Jupiter can range from 4.04 AU to 5.2 AU. To ease comparisons, we use the same scale of distances and solid angles as WMAP (Weiland et al. 2011; Bennett et al. 2013).

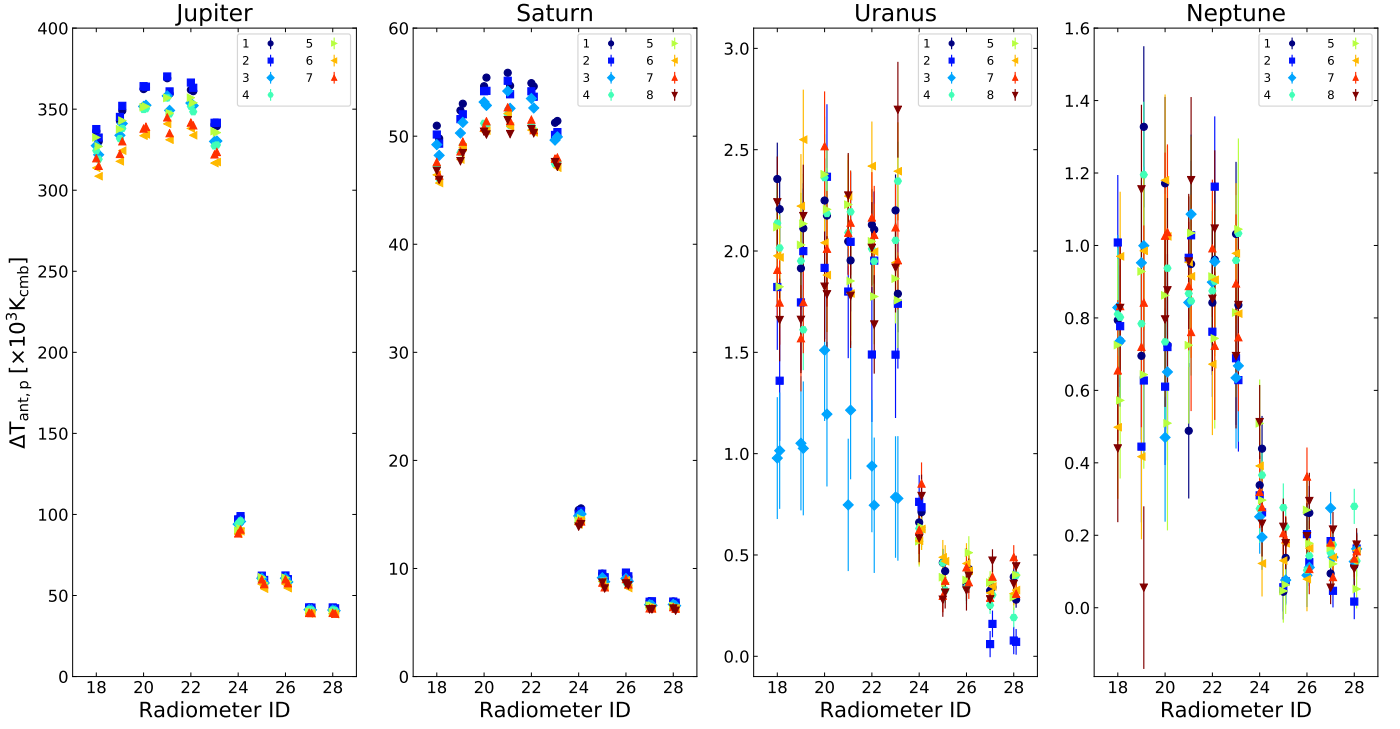


Fig. 6: Values of $\Delta T_{\text{ant},p}^*$ for transits of each planet and radiometer. The X axis is the radiometer index in form $hh.p$ with $hh = 18, 19, 20, 21, 22, 23$ for the 70 GHz channel, 24, 25, 26 for the 44 GHz channel and 27, 28 for the 30 GHz channels. The p index accounts for polarization with 0 for M (Y) polarization and 1 for S (X) polarization. Error Bars account for noise. For Jupiter and Saturn, they are smaller than the size of the symbols.

- The quantity f_{asp} in Eq. (25) is the aspect correction factor described in Sect. A.5; it accounts for the fact that the aspect ratio of the planet seen by *Planck* changes in time.
- The parameter f_{aper} is the aperture correction described in Sect. A.6, and it corrects for the loss of signal in the background ROI.
- The quantity x_η is a correction factor for the lack of numerical efficiency of the beam. As detailed in Sect. A.7, the limited accuracy in the numerical computation of the beam induces a systematic in the measured fluxes at the level of $\sim 10^{-3}$. The precise value of x_η cannot be determined precisely, but it is in the range $\pm f_\eta$ given in Table 1. For this reason, we did not apply the correction, thus assuming $x_\eta = 0$, and we included this in the overall uncertainty. We provide more details in Sect. A.7 and Sect. A.12.

In Planck Collaboration (2014d, 2016c), a correction factor f_{SL} was introduced to account for sidelobes. In this work, this correction is no longer needed, as the GRASP beam model already includes the effect of sidelobes; refer to Sect. A.8 for more details.

Figure 7 shows the derived distribution of the values $\widetilde{\Delta T}_{\text{ant},p}$ (Eq.25). The dispersion within the same frequency channel is significantly reduced for the 70 GHz and nearly flattens, and all the 44 GHz radiometers are now consistent. Geometric corrections do not affect the dispersion in 30 GHz channels significantly.

3.4. Reduction of antenna temperatures to brightness temperatures

The result of our estimate is expected to be the brightness of the planet, expressed as a brightness temperature. The brightness for each radiometer and transit can be derived from $\widetilde{\Delta T}_{\text{ant},p}$ with the formula

$$B_p = \frac{\widetilde{\Omega}_{\text{beam}}}{\widetilde{\Omega}_p} \left(\frac{dB_\nu}{dT} \right)_{\text{cmb}}^{(\text{ba})} \widetilde{\Delta T}_{\text{ant},p} + B_\nu^{(\text{ba})}(T_{\text{cmb}}), \quad (26)$$

with $B_\nu^{(\text{ba})}(T_{\text{cmb}})$ being the correction for the blocked radiation; see also Sect. A.9 and Table 1. Note that the factor $\widetilde{\Omega}_{\text{beam}}/\widetilde{\Omega}_p$ removes the corresponding correction for standardized observing conditions.

We now turn to the problem of properly define what we mean with *brightness temperature* T_b , as several definitions are available in the literature. One widely-used convention is to define a Rayleigh-Jeans (RJ) brightness temperature as

$$T_{\text{b,rj}} = \frac{B_p}{B_{\nu,\text{rj},1}}, \quad (27)$$

where $B_{\nu,\text{rj},1} = 2k_b \nu_{\text{cent}}^2 / c^2$ is the RJ brightness at 1 K estimated at frequency ν_{cent} (see also Table 1). This is the convention followed by WMAP (Weiland et al. 2011; Bennett et al. 2013). On the other side, when data are used to model planetary atmospheres, it is

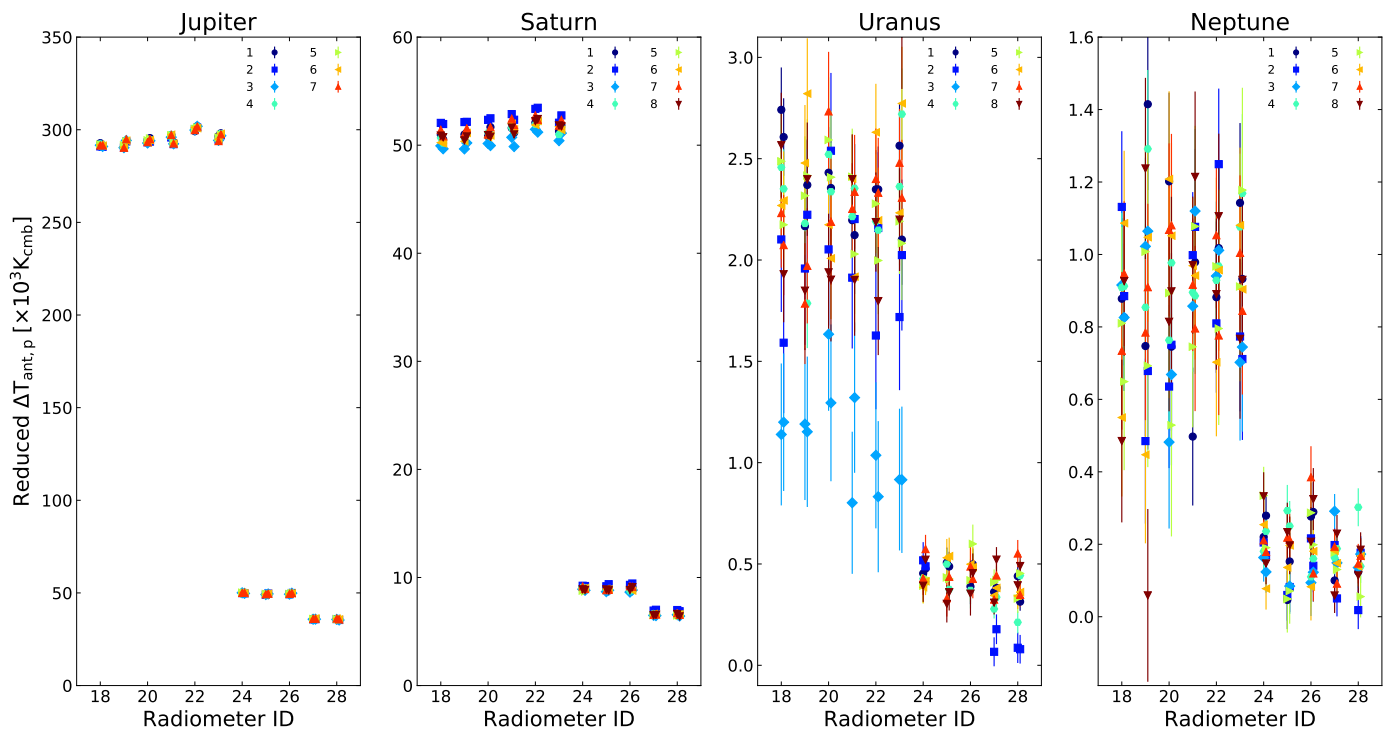


Fig. 7: Values of $\Delta T_{\text{ant,p}}$ after reduction to fiducial observing conditions and standardized Ω_{beam} and Ω_{p} .

better to define T_{b} through the inversion of a planckian curve (de Pater & Dunn 2003; Gibson et al. 2005; de Pater et al. 2016; Karim et al. 2018; de Pater et al. 2019b):

$$B_{\nu}(T_{\text{b,c}}, \nu_{\text{cent}}) = B_{\text{p}}, \quad (28)$$

where “c” denotes one of the frequency channels 30, 44, or 70 GHz. In some cases, the following band-averaged formula can be used to define $T_{\text{b}}^{(\text{ba})}$:

$$B_{\nu}^{(\text{ba})}(T_{\text{b}}^{(\text{ba})}) = B_{\text{p}}, \quad (29)$$

where $B_{\nu}^{(\text{ba})}(T_{\text{b}})$ is the band-averaged SED of a Planckian blackbody. Its inversion is described in Sect. A.11.

Conversion among the different conventions is not difficult, but a detailed model of the instrument bandpass must be taken in account. To simplify the comparison between our results and WMAP’s, and to produce numbers useful for atmospheric modelling, we will provide the three quantities $T_{\text{b,rj}}$, $T_{\text{b,c}}$, and $T_{\text{b}}^{(\text{ba})}$ when needed⁷.

Figure 8 is a summary of the channel-averaged $T_{\text{b}}^{(\text{ba})}$ for each single transit and planet as a function of the quantity D_{p} , the sub-*Planck* latitude at the epoch of the observation as seen from the planet; it represents the planet aspect angle as seen from *Planck*. Since we already include the effect of band-averaging in Eq. (26), we do not need any colour-correction factor.

4. Results

In comparing our results with WMAP’s, we must take in account the different value of the dipole amplitude used by *Planck* and WMAP, as this leads to a mismatch in the absolute calibration level: the *Planck* team used the value $A_{\text{Planck}} = 3364 \pm 2 \mu\text{K}$ (Planck Collaboration 2014d, 2016c, 2018b), while the WMAP team used $A_{\text{WMAP}} = 3355 \pm 8 \mu\text{K}$ (Hinshaw et al. 2009). Therefore, we scaled WMAP’s estimates of $T_{\text{b,rj}}$ by the factor 1.002831. Moreover, WMAP reported $T_{\text{b,rj}}$ rather than $T_{\text{b,c}}$ or $T_{\text{b}}^{(\text{ba})}$. When needed, we used WMAP’s bandpasses to derive $T_{\text{b,c}}$ or $T_{\text{b}}^{(\text{ba})}$ from $T_{\text{b,rj}}$, according to the procedure outlined in Sect. A.19.

Each of the quantities $T_{\text{b,rj}}$, $T_{\text{b,c}}$, $T_{\text{b}}^{(\text{ba})}$ includes the correction for blocking radiation, as explained in Sect. A.9. As an aid for the reader we recall the definition of the main symbols in Table 4.

4.1. Jupiter

Table 5 lists the 7 transits of Jupiter that have been observed by LFI; the last three transits were not considered in the analysis presented by Planck Collaboration (2017). Because of a combination of factors, less samples have been acquired in transits 1 and 4.

⁷ In the abstract we followed the WMAP convention and we quoted $T_{\text{b,rj}}$ as T_{b} .

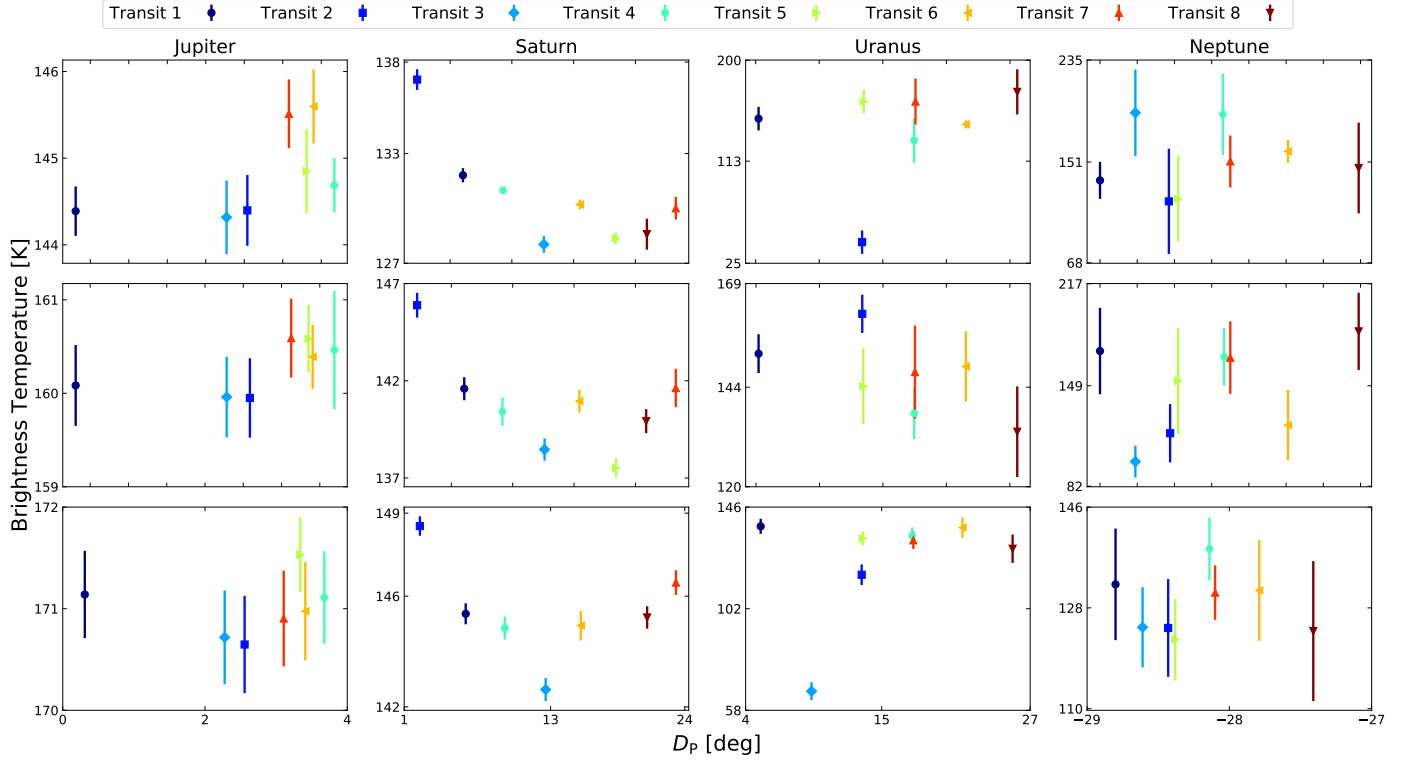


Fig. 8: Values of channel-averaged $T_b^{(ba)}$ per transit as a function of D_P , for 30 GHz (top), 44 GHz (middle), and 70 GHz (bottom) channels. The high variability in the estimates for Saturn is mainly due to the presence of the rings, which have not been removed in this plot.

Table 4: List of symbols used in Sect. 4.

$\tau(\nu), \Delta\nu, \nu_{\text{cent}}, \nu_{\text{cent,eff}}$	Band pass, bandwidth, central frequency and effective central frequency.
Δ, D_P	<i>Planck</i> -planet range and planet aspect angle.
$\Omega_p, \tilde{\Omega}_p$	Planet solid angle and its reference value.
$f_{\text{asp}}, f_{\text{aper}}, f_\eta$	Corrections for planet flattening, beam aperture and beam numerical efficiency.
ΔT_{ant}	Variation of antenna temperature.
T_b	Brightness temperature.
$T_{b,rj}$	Brightness temperature in the Rayleigh-Jeans scale.
$T_{b,c}$	Monochromatic brightness temperature.
$T_b^{(ba)}$	Band-averaged brightness temperature.
$B_v^{(ba)}$	Model band-averaged brightness.
B_p	Measured brightness.

Table 5: Observing conditions of Jupiter per transit.

Transit	Epoch	PJD_Start	PJD_End	Nsmp	EcLon [deg]	EcLat [deg]	GlxLat [deg]	R_h [AU]	Δ [AU]	Θ_p [arcsec]	D_P [deg]
1	2009-10-28	164.66	171.47	8421	317.4	-1.0	-40.3	5.02	4.73	41.65	0.31
2	2010-07-05	413.31	422.26	11040	2.7	-1.3	-61.4	4.97	4.71	41.85	2.56
3	2010-12-11	571.72	581.43	12104	354.2	-1.4	-61.0	4.95	4.79	41.18	2.28
4	2011-08-04	810.48	816.28	6839	39.1	-1.3	-43.2	4.95	4.82	40.93	3.68
5	2012-01-18	971.09	988.22	37035	31.0	-1.1	-48.9	4.98	4.81	41.02	3.34
6	2012-09-07	1208.18	1218.63	22852	75.1	-0.8	-13.3	5.03	4.93	40.03	3.41
7	2013-02-17	1367.85	1384.41	30724	66.7	-0.5	-20.3	5.08	4.88	40.43	3.11

Table 6: Channel-averaged results^a for Jupiter, excluding transits 6 and 7.

ch	ν_{cent} [GHz]	$\nu_{\text{cent,eff}}$ [GHz]	B_p^b [MJy/sr]	$T_{\text{b,rj}}^b$ [K]	$T_{\text{b,c}}^b$ [K]	$T_b^{(\text{ba})b}$ [K]
30	28.40	28.43	3598.2 ± 16.4	144.93 ± 0.17	145.62 ± 0.17	144.69 ± 0.19
44	44.10	44.16	9570.0 ± 23.0	159.76 ± 0.19	160.82 ± 0.19	160.27 ± 0.19
70	70.40	70.36	25866.0 ± 127.8	170.50 ± 0.18	172.18 ± 0.18	171.17 ± 0.19

^a The effect of f_η is not included.

^b The value includes blocked radiation.

All the transits occur near the Equator, with $0.3^\circ < D_p < 3.4^\circ$ (see Sect. 2.4 for the definition of D_p), so that $f_{\text{asp}} < 3 \times 10^{-4}$. The Galactic latitude is always negative, with transit from 1 to 5 between -62° and -40° , transit 6 at -13° and transit 7 approximately at -20° . The last two transits are sufficiently close to the Galactic plane to suffer larger background contamination; this is particularly true at 30 GHz, where Jupiter is weaker and the Galactic background is larger. Figure 8 shows no evident correlations between brightness temperatures and D_p . However, transits 6 and 7 at 30 GHz depart significantly from the average. For this reason, we have limited our analysis to the first 5 transits. In total there are 110 measurements (+44 in transits 6 and 7), of which 20 (+8) at 30 GHz, 30 (+12) at 44 GHz, and 60 (+14) at 70 GHz.

Table 6 reports our values for B_p , $T_{\text{b,rj}}$, $T_{\text{b,c}}$, and $T_b^{(\text{ba})}$. We computed these as the weighted averages of the measurements for each frequency channel across the corresponding set of radiometers, still considering five transits. Adding transits 6 and 7 has a minor impact on the 70 GHz channel: $T_{\text{b,rj}} = 170.40 \pm 0.16$ K, $T_{\text{b,c}} = 172.08 \pm 0.16$ K, $T_b^{(\text{ba})} = 171.07 \pm 0.17$ K. This is a 0.1 K reduction in temperature, and a marginal improvement on the error bars. Since we consider band-averaged quantities, we use the weighted average of the individual ν_{cent} or $\nu_{\text{cent,eff}}$ of each radiometer as the reference frequency. We did not include the effect of the beam numerical efficiency f_η (Sect. A.7) in Table 6, so we added an uncertainty of 0.3%; the calibration uncertainty introduces an additional 0.1% to the error budget.

To derive the averaged values in Table 6, we had to consider some subtleties in the analysis; these are described in Sect. A.12. Of course, averaging B_p and $T_{\text{b,rj}}$ is not the same as averaging $T_{\text{b,c}}$ and $T_b^{(\text{ba})}$, as these are not additive quantities. A more rigorous approach requires to determine the values of $T_{\text{b,c}}$ and $T_b^{(\text{ba})}$ that fit the observed B_p ; this can be done through the minimization of the function of merit in Eq. (A.13), Sect. A.12. We have verified that a simple average agrees with the result of a minimization within the second decimal figure, given the observing conditions of *Planck*/LFI. However, the numbers we report in Table 6 have been derived using the rigorous approach.

Estimating uncertainties is more subtle, as several effects are to be considered. Firstly, there is a large variability in the error bars for $T_{\text{b,rj}}$, which are denoted as $\delta_{\text{rnd}}T_{\text{b,rj}}$: in fact, $\delta_{\text{rnd}}T_{\text{b,rj}}$ varies from 0.06 K to 0.26 K (1σ). These variations can look puzzling, but the transit-to-transit variability in $\delta_{\text{rnd}}T_{\text{b,rj}}$ is highly correlated with the number of samples N_p in the planet ROI: the correlation coefficient between $1/\sqrt{N_p}$ and $\delta_{\text{rnd}}T_{\text{b,rj}}$ is ≥ 0.96 . If we assume that the average of $\delta_{\text{rnd}}T_{\text{b,rj}}$ across a channel is representative of the uncertainties in the data, we should expect overall errors to be $\sim 0.12/\sqrt{28}$ K, $\sim 0.16/\sqrt{42}$ K, and $\sim 0.08/\sqrt{84}$ K, for the 30, 44 and 70 GHz channels respectively. However, this is not what we see in Table 6, as the errors reported here are of the order of 0.2 K, comparable to the worst $\delta_{\text{rnd}}T_{\text{b,rj}}$ on a single measure.

Another indication of some possible systematic error in our data is the scatter of $T_{\text{b,rj}}$ among transits, which exceeds what would be expected from a normal distribution with variance $\delta_{\text{rnd}}T_{\text{b,rj}}^2$. Indeed, the standard deviations for $T_{\text{b,rj}}$ are 0.800 K at 30 GHz, 1.072 K at 44 GHz, and 1.439 K at 70 GHz, while peak-to-peak variations are 3.38 K at 30 GHz, 4.13 K at 44 GHz, and 6.06 K at 70 GHz. Moreover, the distribution of the residuals is not Gaussian.

Fig. 7 shows that the estimates for ΔT_{ant} at 70 GHz are distributed around the mean, but they are not completely compatible with random fluctuations. A closer inspection reveals that most of the effect comes from data collected by the radiometers associated with horns 18 and 22. The averaged $T_{\text{b,rj}}$ from horn 18 deviates by -2.5 K from the average for 70 GHz, while for horn 22 the deviation is $+2$ K; for others, the difference is less than 0.5 K, compatible with the hypothesis of random noise fluctuations. However, removing these samples does not change the results in the table significantly; as an example, we obtained $T_b^{(\text{ba})} = 171.02$ K instead of $T_b^{(\text{ba})} = 170.17$ K (but the 1σ -error decreases from 0.19 K to 0.11 K).

Part of the observed variability across radiometers is intrinsic to the source, given the relatively wide bandwidth of our frequency channels, especially at 70 GHz (Planck Collaboration 2016c). This means that introducing some correction to flatten this effect would introduce another kind of distortion in the data. However when computing uncertainties on channel averaged quantities, the adequacy of usual error propagation formula must be assessed. To validate our estimates for uncertainties given by least-square fits, we used (1) a bootstrap technique, and (2) a MCMC. In case of significant discrepancies, we picked the largest error estimate.

Values of $T_{\text{b,rj}}$, $T_{\text{b,c}}$, and $T_b^{(\text{ba})}$ in Table 6 are very similar, with differences smaller than 2 K ($\sim 1\%$). This happens because Jupiter's brightness temperature is greater than 140 K: since *Planck*'s radiometers measure frequencies below 100 GHz the difference between Planck's law and the RJ's approximation is not large. However, the difference exists and explains the fact that $T_{\text{b,rj}} > T_b^{(\text{ba})}$ at 30 GHz and the opposite at 44 GHz and 70 GHz. In fact, below 30 GHz Planck's law is sufficiently well approximated by the RJ law with brightness scaling as ν^2 ; in this case, the band averaged brightness is larger than the RJ brightness computed at the central frequency. Consequently, $T_{\text{b,rj}} > T_b^{(\text{ba})}$ is needed to explain the same brightness. At higher frequency, the two laws diverge more significantly, and the band-averaged brightness is always smaller than the RJ brightness at central frequency; therefore, $T_{\text{b,rj}} < T_b^{(\text{ba})}$ is needed to explain

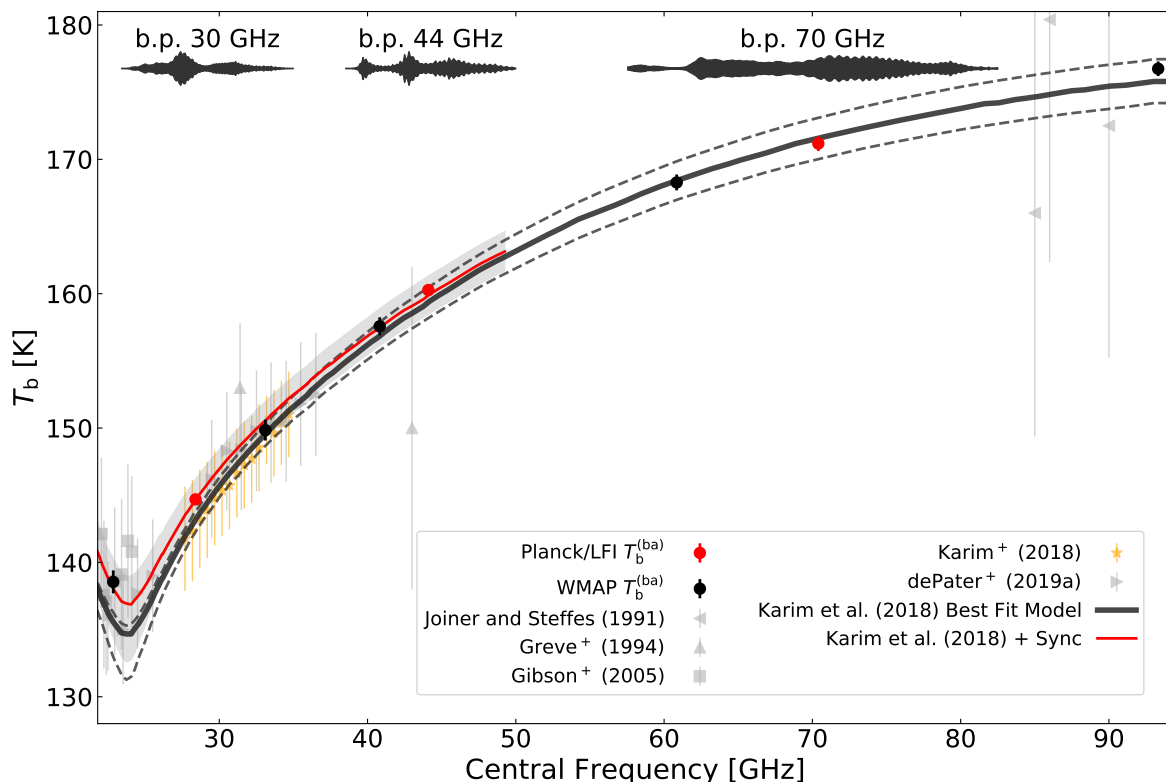


Fig. 9: Comparison of Jupiter measurements made in this paper (red circles) with WMAP (black points, taken from (Weiland et al. 2011; Bennett et al. 2013) and converted to $T_b^{(ba)}$) and with measurements from literature and the RT model by Karim et al. (2018). The model brightness temperature $T_b^{(RT)}$ is plotted as a dark-gray line. Upper and lower dashed lines represent upper and lower limits of model uncertainties as provided in the same paper. The RT model plus the synchrotron emission correction is plotted as a red line; the gray band represents the lower and upper limits. For references of ground-based measurements, see the text. Note that brightness temperatures reported by Gibson et al. (2005) are recalibrated measures originally published by Klein & Gulkis (1978). The violin plots at the top of the figure represent the relative sensitivity to the frequencies inside each bandpass.

the same brightness. The critical frequency where this swap occurs is mainly determined by the bandwidth: for 30 GHz and 44 GHz radiometers, the critical frequency is in the range 29–37 GHz, while for 70 GHz radiometers is 53–60 GHz. The central frequencies for the 30 GHz channel are just below the critical frequencies, while the opposite happens for 44 GHz and 70 GHz radiometers, thus explaining the observed difference. We provide a more quantitative discussion in Appendix A.14.

In Fig. 9 we plot the estimates for $T_b^{(ba)}$ reported in Table 6 and compare them with a selection of results and models available in the literature. Points are plotted at ν_{cent} for each frequency channel. The violin plots at the top give an insight of how $\tau(\nu)$ changes within each frequency channel. The quoted error bars are comparable with the size of the symbols, even including the effect of the $\pm 0.3\%$ f_η correction uncertainty. Black points in the figure represent WMAP’s measurements, taken from Weiland et al. (2011); Bennett et al. (2013) and converted to $T_b^{(ba)}$ as detailed at the begin of this section and in Sect. A.19. WMAP’s results compare well with ours. The plot includes measurements taken from⁸ Joiner & Steffes (1991); Greve et al. (1994); Gibson et al. (2005); Karim et al. (2018); de Pater et al. (2019a). The results from Gibson et al. (2005) are measures provided by Klein & Gulkis (1978) (Tab.II in the paper) and reprocessed. According to the conventions used in this paper they are similar to $T_{b,c}$.

Apart from WMAP, Fig. 9 compares our estimates with other results found in the literature. The few measurements above 40 GHz are consistent with our estimates; the error bars are however large, and the consistency is therefore of little significance. Below 40 GHz, the situation is much better. In particular, the CARMA measurements in Karim et al. (2018) cover the 27.7–34.7 GHz fairly well. Our estimate at 30 GHz is consistent with CARMA, but we see an excess in $T_b^{(ba)}$ of nearly 2 K. As we explain below, this excess is likely due to the presence of a synchrotron contribution to the Jupiter signal that has been removed in the CARMA data (Karim et al. 2018).

The sparse frequency coverage of measurements in the literature makes difficult to quantitatively compare our measurements with that of other authors without adopting an interpolation scheme. But microwave emission of Jupiter can not be reduced to a simple polynomial expression at *Planck*/*LFI* frequencies. In fact, the emissivity observed outside the atmosphere is the result of the radiative transfer of microwave emission produced by different layers within the atmosphere that radiate toward the observer and are extinguished by the traversed layers (see de Pater & Massie 1985; Gibson et al. 2005). At *Planck*/*LFI* frequencies, extinction is dominated by the NH_3 absorption. For this reason, it is interesting to compare our data with representative models in the literature,

⁸ Results from de Pater et al. (1982) and Goldin et al. (1997) are not included, as they are outside the frequency range of interest.

but before discussing the comparison with models, we recall that this paper is devoted to the presentation of Planck/LFI data, and not to a detailed discussion of models for planetary thermal microwave emission.

Here we take as a reference the Jupiter Radiative-Transfer (RT) model described in Karim et al. (2018). The model estimates the full-disk thermal emissivity $T_b^{(RT)}(\nu)$ of Jupiter for wavelengths between 0.3 cm and 4 cm, and it compares well with a number of observations, including CARMA and WMAP 7-yrs. In the plot, $T_b^{(RT)}(\nu)$ is represented by a thick black line. The dashed lines are two further models provided by Karim et al. (2018), which represents an upper and a lower limit for the predicted $T_b^{(RT)}(\nu)$. Our estimates and the model agree very well at 70 GHz, but we overshoot the model at lower frequencies; in particular, at 30 GHz the overshoot is almost 2 K. This happens because at frequencies below 40 GHz the measurement is affected by a small synchrotron emission due to solar high-energy electrons trapped in radiation belts (analogous to Earth's Van Allen belts) within a few Jupiter radii from the planet (Klein & Gulkis 1978).

For Jupiter, the synchrotron emission is mainly concentrated around the equatorial plane, with two emission lobes clearly seen in VLA maps (de Pater 1981; de Pater & Dunn 2003; Kloosterman et al. 2005), and it is polarized at the level of 20–25 % (de Pater & Dunn 2003). Gradual changes over time in the total intensity of the emission have been reported by Klein et al. (2001); Dunn et al. (2003); Kloosterman et al. (2005) at 2.3 GHz and 1.4 GHz. They are mainly connected to secular changes in the density of relativistic electrons in the Jupiter magnetosphere (Dunn et al. 2003; Kloosterman et al. 2005), leading to changes in the synchrotron total intensity but not in its spatial distribution, and to a minor extent to changes in viewing geometry. Abrupt changes in both the intensity and spatial distribution were recorded as a consequence of impacts of minor bodies with Jupiter, as it was the case of comet Shoemaker-Levy 9 in 1994 (de Pater et al. 1995; Klein et al. 2001) and of an unidentified object in July 2009 (Santos-Costa et al. 2011), a few months before the first scan of Jupiter from *Planck*. WMAP did not attempt any removal of this contribution (Weiland et al. 2011), but it is expected to amount to about 1 % of the thermal emission of the disk at 28.5 GHz (Karim et al. 2018). Therefore, this effect is comparable or larger than our error bars.

To include the amount of contamination from synchrotron emission, we follow the formalism in de Pater & Dunn (2003); Weiland et al. (2011); Karim et al. (2018). According to it, the synchrotron emission seen by an observer at Earth has a $\nu^{-0.4}$ spectral dependence, and at the reference frequency of 28.5 GHz the expected synchrotron flux is $F_{\text{sync}} = 1.5 \pm 0.5$ Jy (de Pater & Dunn 2003; Karim et al. 2018), assuming Jupiter as seen at $\Delta = 4.04$ AU corresponding to an $\tilde{\Omega}_{\text{p, sync}} = 4.11075 \times 10^{-8}$ sr. The total brightness is the sum of a thermal and a synchrotron components

$$B_{\text{RT+sync}}(\nu) = B_{\nu} \left(T_b^{(RT)}(\nu) \right) + \frac{F_{\text{sync}}}{\tilde{\Omega}_{\text{p, sync}}} \left(\frac{\nu}{28.5 \text{ GHz}} \right)^{-0.4}, \quad (30)$$

where $T_b^{(RT)}(\nu)$ is derived from the RT model.

The addition of the 1.5 Jy synchrotron emission explains the 30 GHz overshoot. To better constrain our data, we left F_{sync} as a free parameter and fitted it against the 30 GHz and 44 GHz data taken separately and then together. We fitted band averaged brightness from models against the individual $B^{(\text{ba})}$ for each transit and radiometer. This is obtained by replacing $B_{\text{RT+sync}}(\nu)$ and the $\nu^{-0.4}$ dependence with the corresponding band-averaged quantities in Eq. (30):

$$B_{\text{RT}}^{(\text{ba})} = \frac{1}{\Delta\nu} \int_0^{+\infty} d\nu \tau(\nu) B_{\nu} \left(T_b^{(RT)}(\nu) \right), \quad (31)$$

$$F_{\text{sync, 1}}^{(\text{ba})} = \frac{1}{\Delta\nu} \int_0^{+\infty} d\nu \tau(\nu) \left(\frac{\nu}{28.5 \text{ GHz}} \right)^{-0.4}, \quad (32)$$

with $F_{\text{sync, 1}}^{(\text{ba})}$ tabulated for each radiometer in Table 1.

To analyse the effect of the uncertainty on the beam numerical efficiency correction f_{η} , we scaled $B^{(\text{ba})}$ by $(1 \pm f_{\eta})$ obtaining an upper and a lower limit for F_{sync} . Similarly we accounted for the uncertainty in the $T_b^{(RT)}(\nu)$ model by replacing the best fit model in Fig. 9 with the upper or the lower limits models represented by the dashed lines. The best fit F_{sync} and its uncertainties have been derived with the fitting methods already discussed above; we have used a bootstrapping algorithm to validate these uncertainties.

Results are shown in the lower part of Table 7 for the 30 GHz and 40 GHz alone and then taken together. The upper part of the table lists weighted averages of $F_{\text{sync, 1}}^{(\text{ba})} / \tilde{\Omega}_{\text{p, sync}}$ taken across the data sets, and of $B_{\text{RT}}^{(\text{ba})}$ computed for the final model and its lower and upper limits. At 30 GHz the best fit is for $F_{\text{sync}} = 1.50 \pm 0.15$ Jy, to be compared with the expected $F_{\text{sync}} = 1.5 \pm 0.5$ Jy. The uncertainty introduced by the unknown numerical beam efficiency increases the width of the confidence region to $1.15 \text{ Jy} < F_{\text{sync}} < 1.84 \text{ Jy}$. If we use the best fit model of Karim et al. (2018) with the lower or the upper limit, we get $F_{\text{sync}} = 2.83 \text{ Jy}$ and $F_{\text{sync}} = 0.47 \text{ Jy}$ respectively. The 44 GHz suggests a higher value, $F_{\text{sync}} = 2.53 \text{ Jy}$, but the uncertainty is larger; moreover, the upper model would not require any synchrotron component. Combining 30 GHz and 44 GHz gives nearly identical results to the 30 GHz alone. The thermal model plus $F_{\text{sync}} = 1.5 \text{ Jy}$ computed from Eq. (30) is represented by the red line in Fig. 9. The gray band represents the difference between upper and lower limit models. The effect of the uncertainty in the f_{η} correction is comparable to the width of the red dots, and it is not displayed. The inclusion of transits 6 and 7 affects mainly the 30 GHz; in this case, the best fit leads to $F_{\text{sync}} = 1.75 \pm 0.12$.

The presence of some synchrotron could potentially introduce a source of variability for the Jupiter disk averaged brightness. However, apart from the case of transits 6 and 7 at 30 GHz, we have found no other significant correlation with time or with the geometry of observation in our transit-averaged data. Therefore, we may conclude that during our observations Jupiter behaved as a stable microwave source within $\sim 10^{-3}$ over three years, in agreement with Weiland et al. (2011).

Before going further, we want to note that Planck Collaboration (2016c) reports slightly different results for Jupiter. This is caused by a number of small differences in data processing; the most important is the evaluation of f_{aper} , as explained in Sect. A.6.

Table 7: Derivation of F_{sync} from the overshooting of 30 GHz and 44 GHz.

Model ^a		Data Set				
		30 GHz	44 GHz	30 & 44 GHz		
$B_{\text{RT}}^{(\text{ba})}$	model w.a. ^b	3561.7	9518.2	–		"
$B_{\text{RT}}^{(\text{ba})}$	lower model w.a.	3539.0	9447.1	–		"
$B_{\text{RT}}^{(\text{ba})}$	upper model w.a.	3577.1	9584.8	–		"
$F_{\text{sync},1}^{(\text{ba})} / \tilde{\Omega}_{\text{p, sync}}$	w.a.	24.40	20.44	–		"
Fit^c						
F_{sync}	best fit	1.50	2.53	1.58		Jy
"	random error	0.15	0.49	0.14		"
"	fit lower f_{η}	1.15	1.97	1.22		"
"	fit upper f_{η}	1.84	3.09	1.94		"
"	fit lower model	2.43	6.01	0.46		"
"	fit upper model	0.87	−0.73	2.99		"

^a Model for $T_{\text{b}}^{(\text{RT})}(\nu)$. The “lower model” and “upper model” labels indicate the lower and upper limits of the model.

^b W.a. denotes a weighted average over the dataset.

^c The uncertainty in the best fit is divided in three components: (1) random error, (2) upper/lower limits for the effect of the uncertainty on the beam numerical efficiency correction f_{η} , (3) the effect of taking the upper or the lower limit for the model.

Table 8: Observing conditions of Saturn per transit.

transit	Epoch	PJD_Start	PJD_End	Nsmp	EcLon [deg]	EcLat [deg]	GlxLat [deg]	R_{h} [AU]	Δ [AU]	Θ_{p} [arcsec]	D_{p} [deg]
1	2010-01-05	232.80	240.74	9738	184.5	2.3	62.2	9.48	9.28	17.91	6.04
2	2010-06-16	393.89	403.46	11864	177.9	2.4	62.5	9.53	9.45	17.59	2.27
3	2011-01-19	612.40	619.32	8440	197.1	2.5	58.3	9.59	9.36	17.75	12.60
4	2011-07-03	776.55	785.29	10743	190.6	2.5	60.9	9.64	9.62	17.28	9.23
5	2012-01-29	990.40	990.61	31613	209.3	2.5	51.1	9.70	9.50	17.50	18.41
6	2012-07-13	1154.23	1159.87	6807	202.8	2.5	55.1	9.75	9.68	17.16	15.47
7	2013-02-02	1358.62	1363.85	6118	221.1	2.5	42.4	9.80	9.72	17.10	23.28
8	2013-07-23	1529.49	1535.02	6608	214.8	2.4	47.1	9.84	9.74	17.07	20.91

In addition, Planck Collaboration (2016c) compared $T_{\text{b,c}}$ (Eq. 28) with $T_{\text{b,rj}}^{(\text{wmap})}$ (including blocking radiation), which have relative differences of $-5 \times 10^{-4} \div -3 \times 10^{-3}$, equivalent to $-0.07 \div -0.44$ K at 30 GHz, $2 \times 10^{-3} \div 3 \times 10^{-3}$ equivalent to 0.3 K at 44 GHz, and $6 \times 10^{-6} \div 5 \times 10^{-3}$ equivalent to $0.1 \div 0.8$ K at 70 GHz.

4.2. Saturn

Saturn was observed in 8 transits, all of them occurring with $D_{\text{p}} > 0^\circ$; in no cases Saturn crossed the Galactic Plane. The observing circumstances for Saturn are listed in Table 8; note the higher sampling density in transits 2, 4, and 5. Due to changes in the scanning strategy of the *Planck* spacecraft, only horns 24, 27, and 28 observed Saturn during transit 5. Transits from 1 to 4 happened simultaneously with *Planck*/HFI (Planck Collaboration 2017), while transits from 5 to 8 were observed by *Planck*/LFI alone. Transits 1 and 2 occurred near the last two WMAP seasons (Bennett et al. 2013). In total, there are 326 measurements: 96 made by 70 GHz channels, 50 by 44 GHz channels, and 36 by 30 GHz channels.

Table 9 lists the weighted average of $T_{\text{b,rj}}$ and B_{p} for each transit and channel. Errors in the averaged $T_{\text{b,rj}}$ and B_{p} are derived using usual error propagation and are cross-checked both with bootstrap and Monte Carlo simulations. The 44 GHz channel is divided in two sub channels: 44(24) refers to horn 24, and 44(25–26) refers to the average of horns 25 and 26. This split accounts for the fact that the transits in horn 24 and in the pair 25–26 occurs about 5 to 9 days apart. The correction for blocking in both $T_{\text{b,rj}}$ and B_{p} is already introduced. The correction for the beam numerical efficiency f_{η} is not, this adds an uncertainty in $T_{\text{b,rj}}$ or B_{p} of ± 0.30 K (or ± 7.45 MJy/sr) for the 30 GHz channel, ± 0.13 K (or ± 7.81 MJy/sr) for the 44(24) GHz sub channel, ± 0.22 K (or ± 12.12 MJy/sr) for the 44(25-26) GHz sub channel, ± 0.44 K (or ± 66.89 MJy/sr) for the 70 GHz channel independent from the transit down to the second decimal figure. The difference in magnitude for the effect in the 44(24) GHz and 44(25-26) GHz is connected to the location of the feed horns in the focal plane. The horn 24 is between the 30 GHz, while the 25 and 26 are on the opposite site of the focal plane with respect to the horn 24.

The aspect-angle correction we applied to other planets is unreliable in the case of Saturn, because of the presence of the rings. In fact, they emit microwave radiation and partially extinguish the microwave emission radiated from the regions of Saturn’s disk along

Table 9: Table of channel-averaged $T_{b,rj}$ and B_p for Saturn, for each transit.

	Tr. 1	Tr. 2	Tr. 3	Tr. 4	Tr. 5	Tr. 6	Tr. 7	Tr. 8
Channel 30								
w_D	0.9305	0.9693	0.8841	0.9041	0.8686	0.8728	0.8842	0.8722
w_R	0.3409	0.1313	0.7164	0.5261	1.0631	0.8875	1.3762	1.2209
$T_{b,rj}$ [K _{RJ}]	132.17	137.30	128.88	131.56	129.96	131.44	132.46	130.60
error [K _{RJ}]	0.32	0.56	0.41	0.16	0.30	0.24	0.62	0.82
B_p [MJy/sr]	3280.64	3407.65	3198.91	3265.32	3225.74	3262.69	3287.49	3240.65
error [MJy/sr]	37.79	43.81	39.13	27.98	33.23	25.73	44.79	50.35
Channel 44(24)								
w_D	0.9305	0.9693	0.8841	0.9040	0.8686	0.8728	0.8842	0.8722
w_R	0.3404	0.1313	0.7164	0.5266	1.0631	0.8875	1.3762	1.2209
$T_{b,rj}$ [K _{RJ}]	142.00	144.46	139.53	142.14	138.57	142.33	144.02	141.05
error [K _{RJ}]	0.86	0.10	0.72	0.41	0.46	0.32	1.78	0.36
B_p [MJy/sr]	8526.66	8675.34	8378.37	8535.68	8321.22	8547.59	8647.98	8470.06
error [MJy/sr]	125.87	81.92	116.58	99.19	100.20	55.53	182.74	95.68
Channel 44(25–26)								
w_D	0.9303	0.9715	0.8841	0.9055	—	0.8731	0.8845	0.8719
w_R	0.3421	0.1211	0.7170	0.5152	—	0.8816	1.3783	1.2158
$T_{b,rj}$ [K _{RJ}]	140.63	146.20	137.97	138.95	—	140.96	143.27	141.72
error [K _{RJ}]	0.77	0.85	0.68	0.28	—	0.94	1.46	1.02
B_p [MJy/sr]	8381.62	8714.18	8223.17	8281.82	—	8401.98	8539.56	8446.73
error [MJy/sr]	47.68	63.73	57.67	33.61	—	47.08	80.84	61.53
Channel 70								
w_D	0.9304	0.9698	0.8841	0.9044	—	0.8729	0.8843	0.8721
w_R	0.3411	0.1288	0.7170	0.5237	—	0.8863	1.3767	1.2201
$T_{b,rj}$ [K _{RJ}]	144.90	147.93	142.73	144.61	—	145.45	148.41	146.65
error [K _{RJ}]	0.36	0.34	0.40	0.39	—	0.52	0.43	0.39
B_p [MJy/sr]	22019.76	22474.54	21689.96	21981.11	—	22100.77	22558.32	22287.28
error [MJy/sr]	258.39	258.11	265.70	253.51	—	269.20	272.30	280.01

lines of sight intersecting both the ring and the disk. On the other hand, they scatter but do not block background radiation (Weiland et al. 2011).

Following the approach in Weiland et al. (2011); Bennett et al. (2013); Planck Collaboration (2017), we used an empirical model to separate the disk and the ring contribution:

$$T_{b,rj} = \frac{\Omega_{uc} + \sum_{r=1}^7 \Omega_{c,r} \exp(-\tau_r |\csc B|)}{\Omega_p^{(eq)}} T_d + \frac{\sum_{r=1}^7 \Omega_{uh,r}}{\Omega_p^{(eq)}} T_r, \quad (33)$$

where $T_{b,rj}$ are the RJ brightness temperatures quoted in Table 9 for each frequency channel and transit, T_d and T_r are RJ temperatures for the disk and the rings (free parameters of the model), $\Omega_p^{(eq)}$ is the equatorial solid angle of the disk, $\Omega_{c,r}$ is the solid angle of the fraction of the disk that is hidden by the rings, Ω_{uc} is the solid angle of the unimpeded disk, $\Omega_{uh,r}$ is the solid angle of the part of ring r that is not obscured by the disk, and $B = D_p$ is the ring opening angle. All the quantities are calculated at the epoch of the given transit. Rings are numbered starting from the outermost (ring A is $r = 1$) to the innermost (Inner C is $r = 7$). The radii of the rings and their optical depths τ_r are fixed parameters of the model and are taken from Table 10 of Weiland et al. (2011) which follows Dunn et al. (2002). The possibility of considering all the τ_r as free parameters was discussed in Weiland et al. (2011); Bennett et al. (2013); Planck Collaboration (2017) without conclusive results; because of our error bars, we decided to keep them as fixed parameters.

For each set of observations, we derived T_d and T_r through the minimization of the quantity

$$\chi^2 = \sum_t \frac{(w_{D,t} T_d + w_{R,t} T_r - T_{b,rj,t})^2}{\sigma_t^2}, \quad (34)$$

where t runs over the list of transits, and $w_{D,t}$ and $w_{R,t}$ are abbreviations for the coefficients in front of T_d and T_r in Eq. (33). In general, $w_{D,t} + w_{R,t} \neq 1$. The weights $w_{D,t}$ and $w_{R,t}$ are weighted averages of coefficients derived for each radiometer in a given channel and are tabulated in Table 9.

Figure 10 shows $T_{b,rj}$ for each transit and frequency channel as a function of the planet aspect angle D_p . Continuous curves shows the best fit model of Saturn brightness temperature, obtained with different data cuts: (1) all the transits, (2) all but 7 and 8, (3) all but 3, 7, and 8. The reason why we considered transit 3 as peculiar is the occurrence of a massive Saturnian storm during the transit (Janssen et al. 2013). The exclusion of transits 7 and 8 is motivated by the fact that an analysis performed including those transits produces a significantly lower T_r than expected from WMAP and literature measurements. This anomaly is more important at 70 GHz, but it can be traced in the other channels as well. Therefore, at 70 GHz the expectation from WMAP is $T_r \approx 16$ K_{RJ}, while

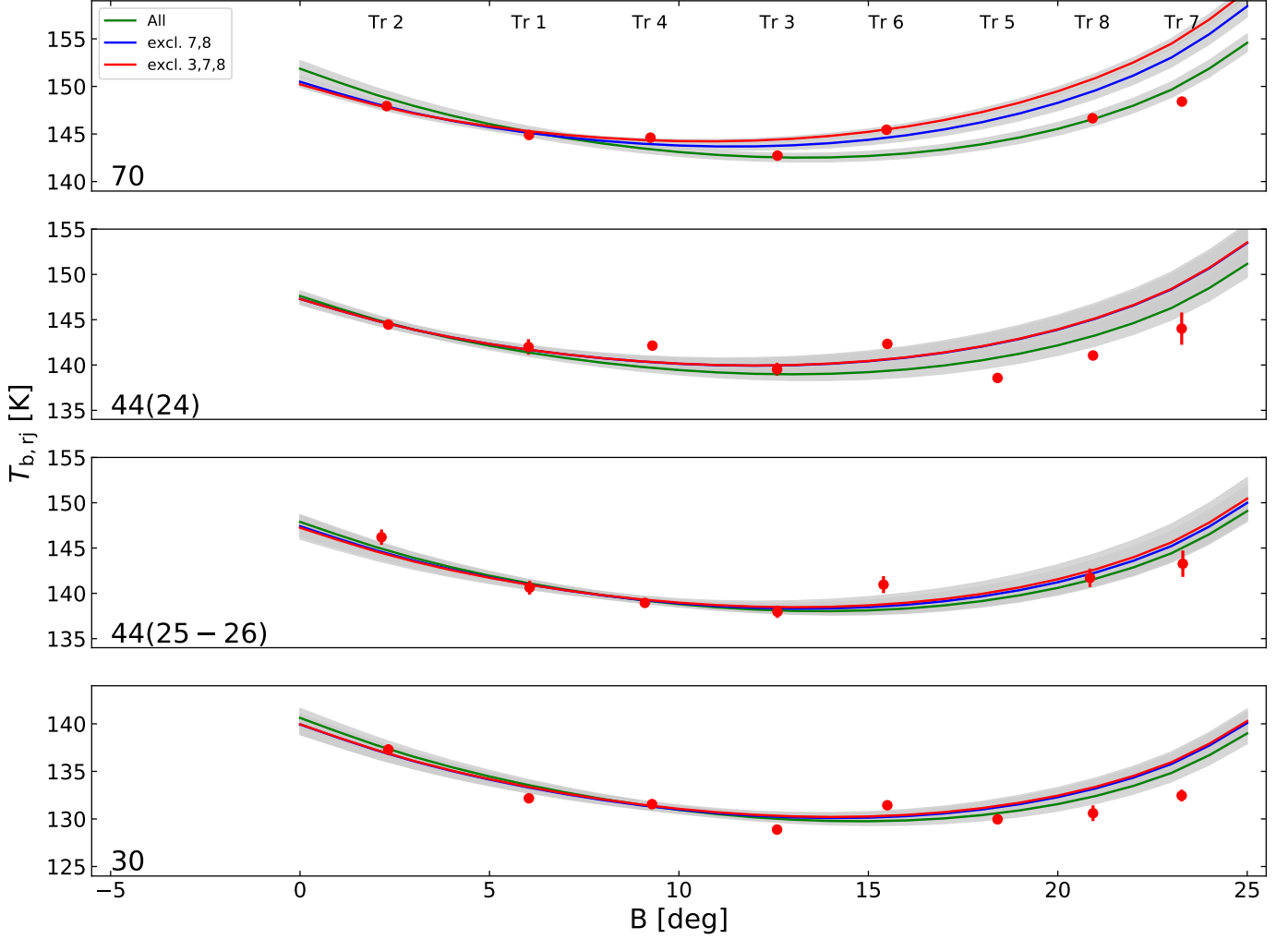


Fig. 10: Saturn $T_{b,rj}$ for 70 GHz frequency channel (first frame from top), 44 GHz frequency channel (second and third frame) and 30 GHz frequency channel (four frame) as a function of D_p . Labels Tr1, Tr2, ..., Tr8 marks the transit from which each observation originates. Continuous curves refers to the best fit models of T_b with different selections of data: All transits, transits 7 and 8 excluded and transits 3, 7 and 8 excluded. The gray bands are 1σ uncertainties in the models.

Table 10: Channel-averaged T_r , T_d , $T_{d,c}$ and $T_d^{(ba)}$ for Saturn from transits 1, 2, 4, 5, and 6.

Channel	ν_{cent} [GHz]	T_r [K _{RJ}]	T_d [K _{RJ}]	$T_{d,c}$ [K]	$T_d^{(ba)}$ [K]
30	28.43	9.21 ± 1.39	139.95 ± 1.07	140.64 ± 1.07	139.74 ± 1.06
44(24)	44.23	13.60 ± 1.58	147.29 ± 0.62	148.35 ± 0.62	147.82 ± 0.62
44(25–26)	44.06	11.59 ± 2.27	147.24 ± 1.27	148.30 ± 1.27	147.81 ± 1.27
70	70.46	16.18 ± 0.74	150.22 ± 0.37	151.95 ± 0.26	151.02 ± 0.26

Planck/LFI data lead to $T_r = 11.6 \pm 1.0$ K_{RJ} (all transits), $T_r = 13.9 \pm 1.0$ K_{RJ} (no 7 and 8), $T_r = 16.2 \pm 0.7$ K_{RJ} (no 3, 7, and 8). Moreover, the reduced χ^2 for the three cases shows a clear progression: $\chi^2_{\nu} = 12.1, 4.1, 0.97$. Inspection of Fig 10 suggests that the reason for this anomaly resides in the fact that $T_{b,rj}$ for transits 7 and 8 is too low when compared to the other transits. We have no explanation for this result, as there were no background sources bright enough to disturb our measurements during those transits, and there were no obvious anomalies in the timelines. We note that the massive Saturnian storm was still visible in 2015 (de Pater et al. 2018); however, without other independent observations to compare, we decided to tag transits 7 and 8 as anomalous. In the remaining discussion, transits 3, 7, and 8 are not used in the fit.

Table 10 gives the list of fitted T_r , T_d for each channel excluding transits 3, 7 and 8. As for the other planets, disk RJ brightness T_d are also converted to $T_{d,c}$ which are equivalent to a $T_{b,c}$ for the other planets, and to $T_d^{(ba)}$ which are equivalent to a $T_b^{(ba)}$. The former are derived from T_d using $T_{d,c} = B_{\nu}^{-1}(\nu_{\text{cent}}, \tilde{B}_{\nu,rj,1} T_d)$, where $\tilde{B}_{\nu,rj,1} = \sum_{t,r} w_{t,r} B_{\nu,rj,1,r} / \sum_{t,r} w_{t,r}$ and $w_{t,r}$ are the weights per transit and radiometer (t, r) used to derive the $T_{b,rj}$ in Table 9 and the latter are obtained through a numerical inversion of $T_d = \int d\nu \tilde{F}(\nu) B_{\nu}(\nu, T_d^{(ba)})$, where $\tilde{F}(\nu) = \sum_{t,r} w_{t,r} \tau_r(\nu) / B_{\nu,rj,1,r} / \sum_{t,r} w_{t,r}$. As our starting point is Table 9, T_d is already corrected

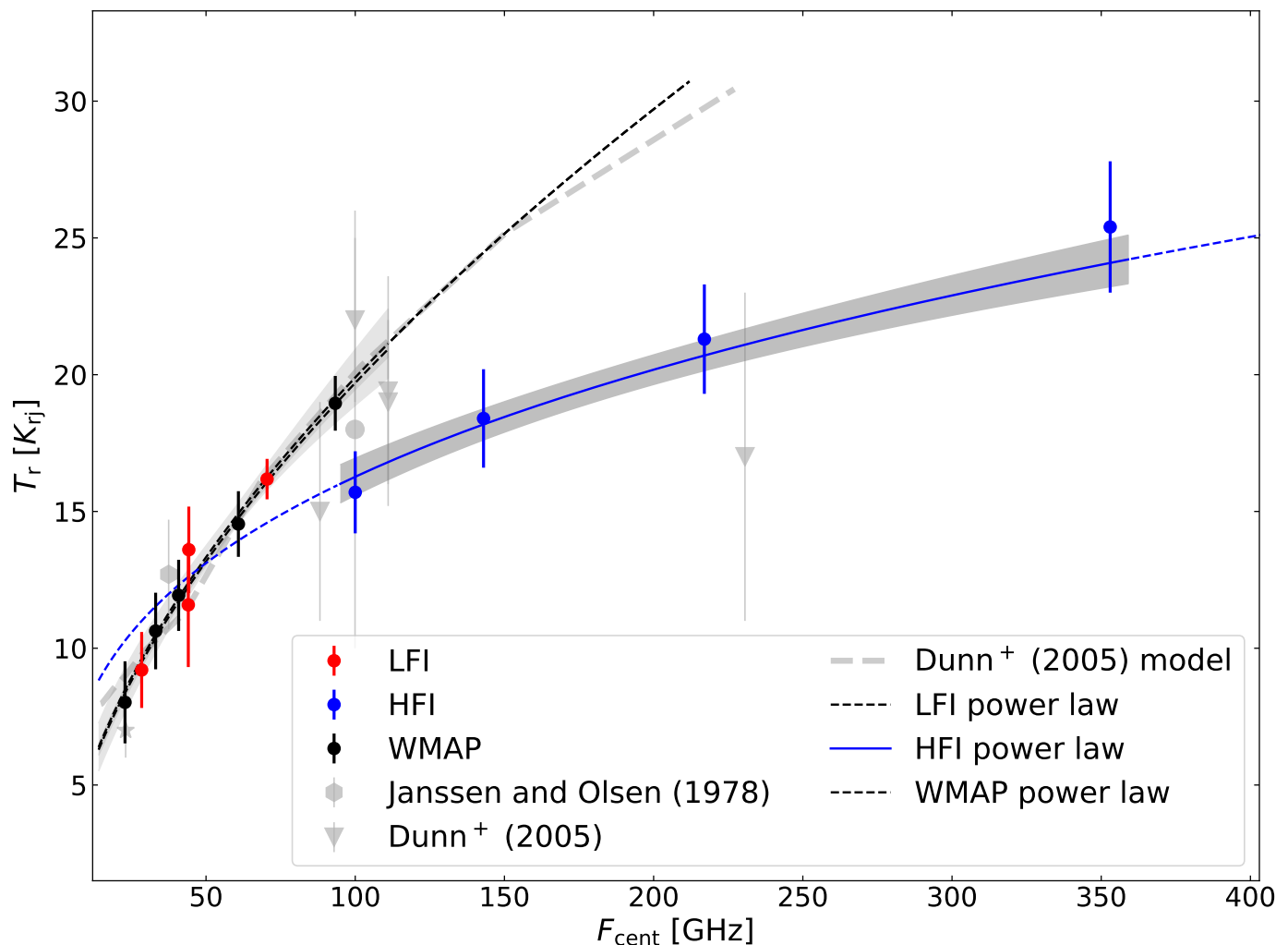


Fig. 11: SED of Saturn rings from *Planck*/LFI (red), *Planck*/HFI (blue) and WMAP (black). Data from previous literature outside WMAP and *Planck* are displayed in light gray (references in the text).

for blocking, we verified that adding the blocking correction to $T_{b,rj}$ has a minor effect on T_r compared to the errorbars. As usual we estimated errors using error propagation, bootstrap and Monte Carlo simulations. We find a good agreement between the three methods, but where differences were relevant, we quoted the largest one. The effect of f_j is equivalent to add a systematic uncertainty of ± 0.35 K for the 30 GHz channel, ± 0.13 K for the 44(24) GHz sub-channel, ± 0.26 K for the 44(25-26) GHz sub-channel, and ± 0.46 K for the 70 GHz channel at T_d , $T_{d,c}$ and $T_d^{(ba)}$. For T_r the uncertainty is $\pm 3.5 \times 10^{-3}$ K for the 30 GHz channel, $\pm 8.6 \times 10^{-2}$ K for the 44(24) GHz sub-channel, $\pm 2.0 \times 10^{-2}$ K for the 44(25-26) GHz sub-channel, $\pm 4.6 \times 10^{-2}$ K for the 70 GHz channel.

Figure 11 compares T_r in Table 10 (red markers) with results from Weiland et al. (2011), Bennett et al. (2013) (black markers), and Planck Collaboration (2017) (blue markers). Data from literature are presented as gray marks (Janssen & Olsen 1978; Schloerb et al. 1979b,a; Epstein et al. 1980; Dunn et al. 2005). Moreover, we compared our results with the model of Dunn et al. (2005). Our estimates for Planck/LFI compare well with the other available data. In particular, both *Planck*/LFI and WMAP measurements fit well the result of Janssen & Olsen (1978) near 40 GHz and with Dunn et al. (2005) at 100 GHz and 110 GHz. Also both for the case of Planck/LFI and WMAP T_r matches a power law of the form $T_r = A\nu_{\text{cent}}^\alpha$, consistent with the model of Dunn et al. (2005). For WMAP $A = (1.35 \pm 0.12) \text{ K}_{\text{RJ}}$ and $\alpha = 0.58 \pm 0.02$ (black dashed line), while for *Planck*/LFI $A = (1.36 \pm 0.55) \text{ K}_{\text{RJ}}$ and $\alpha = 0.58 \pm 0.10$ (black dashed line). It is interesting to note that *Planck*/HFI, exhibits a less steep power law with $A = (3.88 \pm 0.92) \text{ K}_{\text{RJ}}$ and $\alpha = 0.311 \pm 0.044$ (blue line), predicting a lower T_r at 70 GHz, an higher T_r at 30 GHz; the agreement at 44 GHz is much more significant. When taken together, Planck/LFI, WMAP, and *Planck*/HFI seems to suggest a change in slope around 100 GHz, but the only measure in a significant disagreement with *Planck*/HFI seems the one from WMAP 90 GHz. The remaining data from literature are not sufficiently accurate to take a decision. This could be an interesting point for a future observing campaign in the 50–150 GHz frequency range.

Figure 12 compares $T_d^{(ba)}$ for *Planck*/LFI with WMAP (Weiland et al. 2011; Bennett et al. 2013) and *Planck*/HFI (Planck Collaboration 2017). There is a good agreement between the three datasets, despite our data seem to prefer a slightly warmer disk than WMAP's. Older data taken from literature (Klein et al. 1978; de Pater & Dickel 1991; Greve et al. 1994; Goldin et al. 1997;

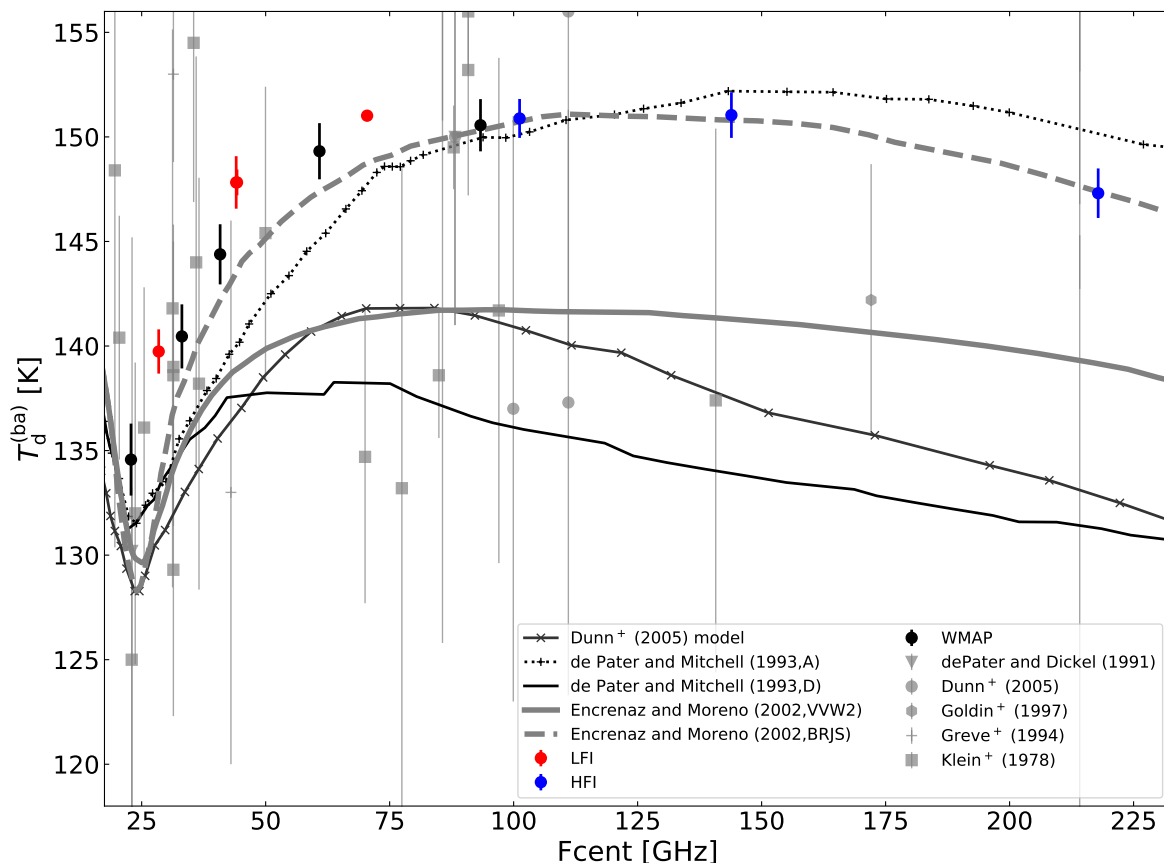


Fig. 12: SED of Saturn disk from *Planck*/LFI (red), *Planck*/HFI (blue) and WMAP (black). The model labelled dePater and Mitchell (1993,A) does not include clouds, while dePater and Mitchell (1993,D) included clouds. For other details about the other models see the text.

Dunn et al. 2005)⁹ are very sparse in frequency coverage and exhibit wider error bars. In the frequency interval 50–150 GHz, measurements from the literature span the range 135–160 K, but most of the measurements are in the lower side of the interval, while measurements from WMAP and *Planck* prefer the upper side. The reason could be in the absolute calibration of those old observations, as an absolute calibration error of the order of ten percent is often quoted in these works, and observations are not usually calibrated against the same sources. This is the opposite of WMAP and *Planck*, which share the same calibration.

Most of the models proposed in literature underestimate the combined WMAP and *Planck* data; some of those models are presented in Fig. 12. In all these models, the atmosphere is assumed to have abundances of NH_3 , H_2O , H_2S , CH_4 enhanced with respect to the Sun by a factor 3, 5, 11 and 5, respectively. The first model presented in the figure (de Pater & Mitchell 1993, labelled “de Pater and Mitchell (1993,A)”) (dashed line with crosses) does not include any contribution from cloud absorption, and it underestimate the observed brightness below 90 GHz; above this frequency, it matches our data, but it overestimates the majority of the older measurements. The inclusion of clouds with NH_3 ice, H_2O liquid and ice, NH_4SH ice leads to the model labelled as “de Pater and Mitchell (1993,D)” (full black line), which underestimates our measurements. Similar behaviour appears with the models in van der Tak et al. (1999), with abundances of NH_3 , H_2O , H_2S , CH_4 enhanced by a factor 1.9, 4, 11 and 4 with respect to Solar values (not displayed here for brevity), and in Dunn et al. (2005) which is an improved version of the nominal model in de Pater & Mitchell (1993). Encrenaz & Moreno (2002) proposed two models with two different profiles for the extinction of the NH 1.28 cm line: BRJS (Ben-Reuven 1966; Joiner & Steffes 1991) and VVW2, a Van Vleck-Weisskopf profile (de Pater & Massie 1985; Lellouch & Destombes 1985; Moreno 1998). The authors favour VVW2, since it better fits data in literature, with the caveat that its model line profile heavily underestimates *Planck* and WMAP data, while the BRJS fits them much better. We note that neither de Pater & Mitchell (1993) nor Dunn et al. (2005) include the PH_3 absorption band at 263 GHz, which is instead present in the last two models.

In Planck Collaboration (2017), a model named *ESA2 model* has been used to compare *Planck*/HFI results with WMAP and earlier *Planck*/LFI results. The predicted brightness temperature is very similar to the one predicted by the model in Encrenaz & Moreno (2002), with VVW2 profile. The work provides also uncertainty limits; in particular, the upper limit is very similar to the Encrenaz & Moreno’s model with BRJS profile; this upper limit fits both WMAP and *Planck* data. Unfortunately no references or details are given about this model, and for this reason it is not presented here.

⁹ Data presented in Schloerb et al. (1979b); Epstein et al. (1980); Cunningham et al. (1981); Grossman et al. (1989) are outside our frequency range.

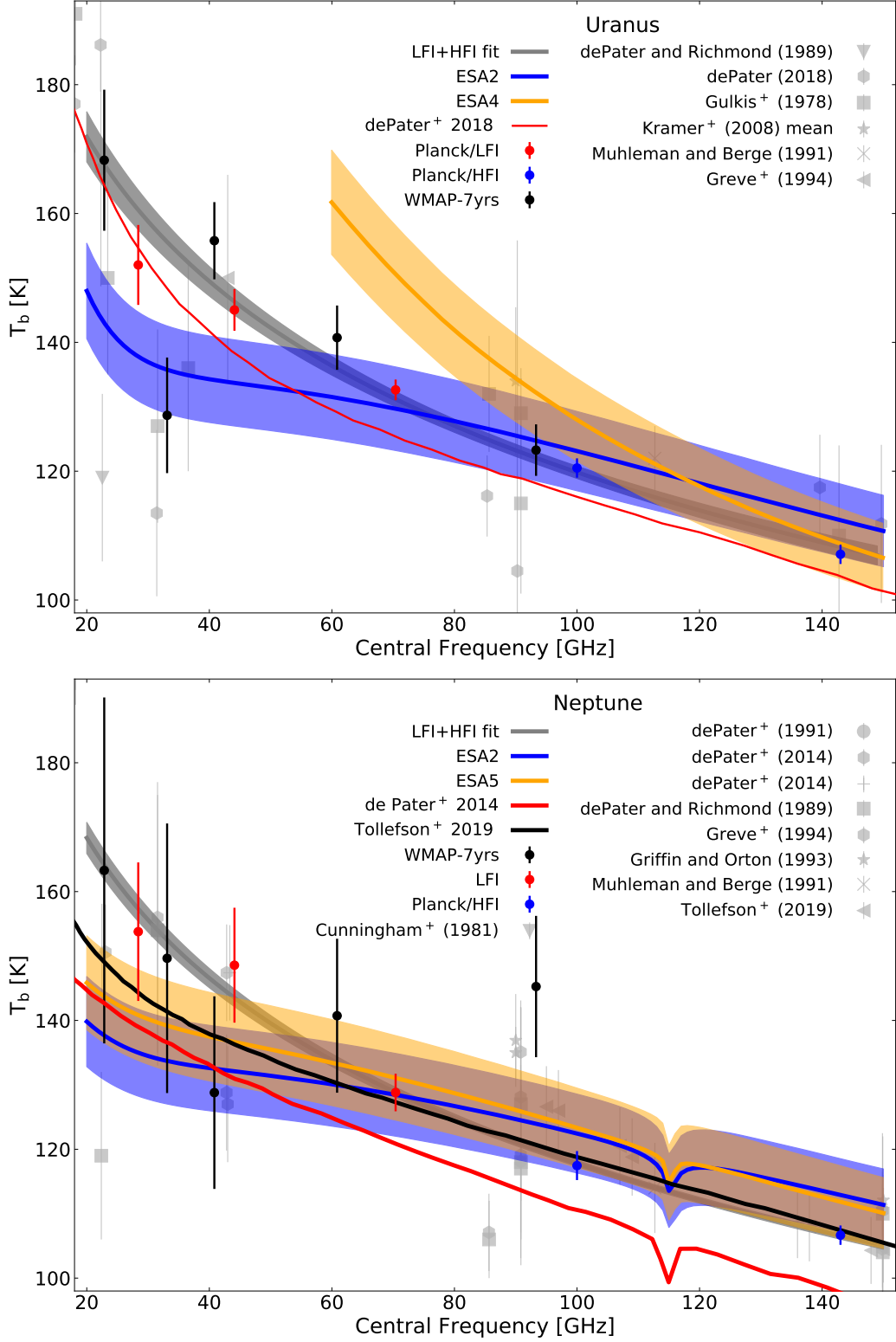


Fig. 13: $T_b^{(ba)}$ for Uranus (top) and Neptune (bottom), compared with representative models.

4.3. Uranus and Neptune

Tables 11 and 12 describe the observing conditions for Uranus and Neptune. There are 8 transits in which both planets are observed; all the cases transits occurred far from the Galactic Plane. For both Uranus and Neptune, the signal is very weak, especially at 30 GHz and 44 GHz, and they are therefore difficult to detect. For Uranus, $\Delta T_{\text{ant,p}}^*$ is in the range $6 \times 10^{-5} \div 5 \times 10^{-4} K_{\text{cmb}}$ at 30 GHz, $3 \times 10^{-4} \div 9 \times 10^{-4} K_{\text{cmb}}$ at 44 GHz, and $7 \times 10^{-4} \div 3 \times 10^{-3} K_{\text{cmb}}$ at 70 GHz, While for Neptune $\Delta T_{\text{ant,p}}^*$ is in the range

Table 11: Observing conditions of Uranus per transit.

Transit	Epoch	PJD_Start	PJD_End	Nsmp	EcLon [deg]	EcLat [deg]	GlxLat [deg]	R_h [AU]	Δ [AU]	Θ_p [arcsec]	D_p [deg]
1	2009-12-09	205.26	214.03	10727	352.6	-0.8	-60.1	20.10	20.01	3.52	5.21
2	2010-07-02	410.43	418.96	10510	0.5	-0.8	-60.9	20.09	19.93	3.54	13.38
3	2010-12-14	575.50	584.31	10914	356.5	-0.8	-60.8	20.09	20.02	3.52	9.32
4	2011-07-07	780.66	788.84	10081	4.4	-0.7	-60.6	20.08	19.90	3.54	17.46
5	2011-12-25	952.75	958.41	6487	0.6	-0.7	-60.9	20.08	20.11	3.51	13.48
6	2012-07-09	1150.09	1155.72	6683	8.4	-0.7	-59.8	20.07	19.90	3.54	21.53
7	2012-12-27	1321.50	1327.14	6762	4.5	-0.7	-60.6	20.06	20.08	3.51	17.55
8	2013-07-13	1518.76	1524.31	6588	12.3	-0.7	-58.6	20.05	19.89	3.54	25.58

Table 12: Observing conditions of Neptune per transit.

Transit	Epoch	PJD_Start	PJD_End	Nsmp	EcLon [deg]	EcLat [deg]	GlxLat [deg]	R_h [AU]	Δ [AU]	Θ_p [arcsec]	D_p [deg]
1	2009-11-03	171.04	177.90	8439	323.5	-0.4	-44.5	30.03	29.83	2.29	-28.80
2	2010-05-19	366.56	374.99	10239	328.5	-0.5	-48.0	30.02	30.04	2.27	-28.43
3	2010-11-06	538.33	545.34	8705	325.7	-0.5	-46.1	30.02	29.81	2.29	-28.61
4	2011-05-22	734.34	742.96	10462	330.7	-0.5	-49.6	30.01	30.03	2.27	-28.14
5	2011-11-19	917.18	922.35	6192	328.0	-0.6	-47.8	30.00	29.98	2.28	-28.38
6	2012-06-05	1115.51	1122.59	8597	333.0	-0.6	-51.1	30.00	29.79	2.29	-27.79
7	2012-11-23	1286.19	1293.91	9436	330.2	-0.6	-49.3	29.99	30.02	2.27	-28.10
8	2013-06-08	1483.26	1490.15	8343	335.2	-0.7	-52.5	29.99	29.78	2.29	-27.41

Table 13: Channel-averaged results for Uranus.

ν_{cent} [GHz]	B_p [MJy/sr]	$T_{\text{b,rj}}$ [K]	$T_{\text{b,c}}$ [K]	$T_{\text{b}}^{(\text{ba})}$ [K]
28.4	3781.1±155.8	152.3±6.3	153.0±6.3	152.0±6.2
44.1	8648.3±193.3	144.5±3.3	145.5±3.3	145.0±3.2
70.4	20032.7±265.6	131.7±1.6	133.4±1.6	132.6±1.6

Table 14: Channel-averaged results for Neptune.

ν_{cent} [GHz]	B_p [MJy/sr]	$T_{\text{b,rj}}$ [K]	$T_{\text{b,c}}$ [K]	$T_{\text{b}}^{(\text{ba})}$ [K]
28.4	3827.2±267.1	154.1±10.8	154.8±10.2	153.8±10.8
44.1	8852.7±538.0	148.0± 9.0	149.1± 9.0	148.6± 8.9
70.4	19445.7±458.5	127.9± 2.9	129.6± 2.9	128.2± 2.9

$2 \times 10^{-5} \div 3 \times 10^{-4} K_{\text{cmb}}$ at 30 GHz, $4 \times 10^{-5} \div 5 \times 10^{-4} K_{\text{cmb}}$ at 44 GHz, and $6 \times 10^{-5} \div 1.3 \times 10^{-3} K_{\text{cmb}}$ at 70 GHz. In some cases, the result of the fit is $\Delta T_{\text{ant,p}}^* \leq 0$, which means that the planet is not detected: for Uranus, this occurs in transits 2 and 3 for horns 25 and 26, and in transit 3 for horns 24, 27, and 28; for Neptune, this occurs in transit 3 for radiometers 25M and 28M. We have decided not to include these data in our analysis.

Figure 8 shows that the scatter in the channel averages for each transit are consistent with the error bars, except for $T_{\text{b}}^{(\text{ba})}$ at 30 GHz in transit 2, and at 70 GHz in transit 3. We removed these two data points before computing the channel averaged results presented in Table 13 (Uranus) and in Table 14 (Neptune). It is known that Uranus has a significant time variability in microwave over a time scale of decades, mainly connected to the change in the D_p of the observation (Klein & Hofstadter 2006; Kramer et al. 2008a). Kramer et al. (2008a) reported a relative variation of 0.5%/year or 0.1% at 90 GHz for one degree of variation of D_p . Assuming that the same numbers are valid at 70 GHz and a time span between our observations of about 3.6 years, corresponding to a span of about 20.4° in D_p , we expect to detect a change of the order of 2–2.6%. As shown in Fig. 8, the scatter in our data is larger than this effect; therefore, we decided not to consider it.

Figure 13 compares *Planck*/LFI Uranus and Neptune $T_{\text{b}}^{(\text{ba})}$ measurements (in red) with *Planck*/HFI measurements at 100 GHz and 143 GHz (in blue) from Planck Collaboration (2017), and WMAP 7-year measurements converted to $T_{\text{b}}^{(\text{ba})}$ (in black). In addition we show a selection of measurements published in the past literature (in gray). Data for Uranus are taken from Gulkis et al. (1978); de Pater & Richmond (1989); Muhleman & Berge (1991); Greve et al. (1994); de Pater (2018)¹⁰; for Kramer et al. (2008a) we only show the average of the data. For Neptune data are taken from Cunningham et al. (1981); de Pater & Richmond (1989); de Pater et al.

¹⁰ Data from (Cunningham et al. 1981; Griffin & Orton 1993; Klein & Hofstadter 2006) are not shown here since they are outside the frequency range of interest.

(1991); Muhleman & Berge (1991); Griffin & Orton (1993); Greve et al. (1994); de Pater et al. (2014); Tollefson et al. (2019). Our measurements for both Uranus and Neptune are in general agreement with WMAP, *Planck*/HFI, and the past literature.

At the opposite of Jupiter and Saturn, where the 1.3 cm NH₃ inversion line and PH₃ transitions significantly affect the spectrum, it has been observed that Uranus and Neptune spectra in the 20–150 GHz smoothly decrease with frequency (de Pater et al. 1991; Encrenaz & Moreno 2002). A simple law can be used to transfer observations from one frequency to the other, similar to the fourth-order polynomial in log₁₀ ν provided by Griffin & Orton (1993); in the range of frequencies of interest for this work, this can be reduced to the simpler form

$$T_b = A \log_{10} \left(\frac{\nu}{100 \text{ GHz}} \right) + B, \quad (35)$$

with A and B free parameters. For Uranus $A = -74.5 \pm 31.6$ K, $B = 118.9 \pm 0.9$ K, and for Neptune $A = -72.3 \pm 9.9$ K, $B = 117.8 \pm 0.2$ K. The corresponding fit is shown as a gray band in the figures. For Uranus, the discrepancy between the 70 GHz datum and WMAP is ~ 2 K, a bit more than 1%. On the contrary, for Neptune the WMAP V and W bands overestimate both our number at 70 GHz and *Planck*/HFI's estimate at 100 GHz.

At odd with the expected smooth T_b variation with frequency, the WMAP team noted that T_b in their Ka band drops with respect to their K and Q bands (Weiland et al. 2011); the significance of this drop is reinforced by comparison with other observations in the literature. Our results does not disconfirm this finding, as our measure at 44 GHz agree with WMAP Q band, while the 30 GHz datum is between between WMAP K and Ka bands. The combination of all of the observations suggests the presence of a drop in the thermal emission of Uranus that is centered at about 30 GHz, with a width of about 5 GHz and a depth of 20–50 K. However, the uncertainty in the magnitude of the drop is quite large, data in literature have wide error bars and use different calibrations; therefore, we think that more data are needed to validate the existence of this spectral feature.

Models of the microwave emission of Uranus and Neptune are available in Griffin & Orton (1993); Kramer et al. (2008b); Griffin et al. (2013); Bendo et al. (2013). Here we consider the models in de Pater (2018) for Uranus and in de Pater et al. (2014); Tollefson et al. (2019) for Neptune, together with ESA's models used for the calibration of *Herschel*; the latter has a quoted 5% uncertainty (Moreno 1998; Teyssier & Marston 2017)¹¹. They are included in our figure, as they are important for the inter-calibration between *Herschel* and *Planck* (Bertincourt et al. 2016; Müller et al. 2016; Planck Collaboration 2017).

The model of de Pater (2018) for Uranus assumes abundances of H₂O, H₂S, CH₄ enhanced of a factor ten with respect to Solar abundances of O, S and C. Ammonia is kept at solar N abundance and is captured in NH₄SH clouds; therefore, it is depleted above the corresponding atmospheric layer. According to this model, at our frequencies opacity is mainly due to H₂S absorption and collisionally induced absorptions from H₂. The figure shows that the model essentially matches our scaling law and only slightly underestimates our 44 and 70 GHz data; it does not predict any *drop* around 30 GHz.

The ESA2 model for Uranus (light-blue), is an updated version of the model in Moreno (1998) used for the calibration of *Herschel*. It was used to validate *Planck*/HFI data and for comparison with WMAP (Planck Collaboration 2017). Our 70 GHz measure is well in agreement with this model, and even the 30 GHz datum agrees with this model. It is interesting to note that the model predicts a decrease of signal around 30 GHz, but it fails to follow the pattern of the spectrum below 45 GHz. Unfortunately, few details are provided for this model, so it is not possible to push the analysis further. After the release of the ESA2 model, the *Herschel* collaboration proposed another model of the spectrum of Uranus named ESA4 (in orange in the plot), which includes observations from Spitzer (Orton et al. 2014) and extended down to 60 GHz. It is evident that the model significantly overestimates the brightness below 100 GHz.

For Neptune, we considered the model in de Pater et al. (2014) (in red). The model featured abundances of H₂S, H₂O and CH₄ enhanced by a factor 30 with respect to Solar abundances of S, O and C, and a wet lapse rate. The model matches our scaling law but underestimated T_b of about 10%.

We included in our analysis the model in Tollefson et al. (2019)¹² (black continuous line). It features an abundance of H₂S, CH₄ and H₂O that is 30 times the proto-Solar abundance. The model fits the data for *Planck*/LFI 70 GHz and *Planck*/HFI 100 GHz and 144 GHz quite well, but it underestimates the measurements at 30 GHz and 44 GHz.

The ESA2 and ESA5 models are also shown in the figure respectively as blue and a orange lines. ESA5 was used to validate the *Planck*/HFI data, but it has been not used for the final calibration of *Herschel*¹³. As already noted in Planck Collaboration (2017), the model slightly overestimated the brightness temperature in the range 70–200 GHz and underestimated our 30 GHz and 44 GHz data. It is interesting to note the good agreement between ESA2 and our measurement at 70 GHz.

For Neptune, both ESA2 and ESA5 models marginally fit our results above 70 GHz, and ESA5 looks slightly better than ESA2.

5. Conclusions

We analysed the data in the *Planck* 2018 public data release to characterize the emission of the planets Jupiter, Saturn, Uranus, and Neptune in the frequency range 30–70 GHz, using all the data acquired by the LFI instrument during its 4-year-long lifetime (August 2009–October 2013). LFI observed 7 times Jupiter, and 8 times the other planets. In the past, just part of those transits have been fully analysed in a self-consistent manner. On the contrary, we have treated all the observations in a fully homogeneous manner. Moreover, we used our improved knowledge of the beam and band-passes to refine our earlier analysis.

In each transit, a planet was observed by *Planck*/LFI for a few hours rather than days or weeks as in the case of WMAP. Within each transit, the cumulative integration time is about few seconds per planet, transit, and radiometer.

¹¹ <https://www.cosmos.esa.int/web/herschel/calibrator-models>.

¹² The model labelled *30xS dry* in their Fig. 3.

¹³ According to the Readme file in the *Herschel* models repository.

In the case of Jupiter and Saturn, the sensitivity of *Planck*/LFI allowed us to reduce the impact of instrumental white noise to a small amount, and the dispersion of our measurements within each frequency channel after geometrical corrections shows a residual variability larger than the noise. Calibration uncertainties on individual radiometers could be a source of such variability: in particular, we cannot exclude that part of the radiometer-by-radiometer variability we observed in our sample of Jupiter’s observations could be connected to uncertainties in the model of the bandpass of each radiometer. This could introduce small differences between the calculated radiometers central frequencies, bandwidths or higher order bandpass moments and the real ones. In principle, by comparing measures of a bright source, like Jupiter, with a well-calibrated model or set of measures from another instrument, it would be possible to derive a correction for this effect. But if blindly applied, this method will force each other possible residual systematic in this correction. For this reason and the lack of a sufficiently accurate model of Jupiter emissivity, including non-thermal emission, we did not attempt to derive this kind of correction in this work. We guess that improved calibration methods, like the ones described in The BeyondPlanck Collaboration (2020), will improve this result.

Despite the difference in the time span of observations, our results are directly comparable to WMAP observations (Weiland et al. 2011; Bennett et al. 2013), which were obtained in a similar range of frequencies. In particular, we confirm the good agreement between the *Planck*/LFI and WMAP estimates of Jupiter’s SED. Our results improve the frequency coverage in the range 20–90 GHz. A comparison with existing models below 70 GHz allowed us to estimate Jupiter’s synchrotron contribution in the 30 GHz channel in the range 0.9–2.4 Jy. As *Planck*/LFI and *Planck*/HFI cover separate ranges of frequencies, to compare them we had to rely on far-infrared emissivity models for giant planets. The result of our comparison shows a good agreement between the measurements of the two instruments.

Our estimates for Saturn’s disk SED are in agreement with WMAP at 30 GHz, but our results favour a slightly warmer disk at 44 GHz and 70 GHz. With the present knowledge of the instrument it is not possible to assess whether the difference is due to some systematic in either *Planck*/LFI or WMAP or if it is connected to the fact that WMAP observations were centered at negative planetocentric latitudes, while *Planck*/LFI observations were centered at positive latitudes. Given the large error bars of older measurements in literature, we can only say that our measures agree with most of the older ones. We compared our Saturn’s measurements with known models published in the literature. All of them but two significantly underestimated the SED in the frequency range considered here. About rings, we may note the excellent agreement of *Planck*/LFI with both WMAP and existing estimates for frequencies below 100 GHz. Data below 100 GHz show some discrepancy with *Planck*/HFI, but the existing data does not allow to assess the significance of this mismatch.

Measures for Uranus and Neptune have very low S/N. For some transit and/or radiometer, confusion noise prevented a proper detection: consequently, error bars are larger than for Jupiter and Saturn, although they agree with those in literature. In particular, our results are in agreement with WMAP and *Planck*/HFI at 100 GHz and 143 GHz. We compared a selection of existing models for the microwave emissivity of Uranus and Neptune with our data plus WMAP and *Planck*/LFI. They show a good agreement in the 100–143 GHz range but significant discrepancies below 100 GHz. In particular, Uranus’ model presented in de Pater (2018) and Neptune’s model found in Tollefson et al. (2019) show a better agreement with our data. For observers willing to use these planets as calibrators, we advise that a simple power-law is quite good at modelling the dependence on T_b for Uranus and Neptune in the frequency range 20–143 GHz within the current errorbars.

In earlier generations of CMB experiments, giant planets have been considered good beam calibrators and have been used as calibration sources between different experiments, thanks to their high signal to noise ratio (Weiland et al. 2011; Bennett et al. 2013; Planck Collaboration 2014d, 2016c). Planetary observations will likely maintain the same importance in future missions, such as the planned *LiteBIRD* mission (Hazumi et al. 2019). The increased demand for accurate and sensitive CMB measurements will necessarily require more accurate models for the analysis of planetary emission in the microwave range. Outer planets, in particular Jupiter and Saturn, have complex spectra and no simple scaling law are going to work, especially when combining data from detectors with different bandpasses. In this case, people should use reliable models of planetary emissivities (including both thermal and non thermal components); however, current models have uncertainties larger than the measurement errors. An observing campaign with ground based instruments, coupled with progresses in modelling, could solve this problem.

Acknowledgements. This work is based on the 2018 Release of *Planck*/LFI data. The writers acknowledges the support of: *Planck* Collaboration, ESA, ASI, CNR, Università di Milano and INAF (Italy); CNES and CNRS/INSU-IN2P3-INP (France); NASA and DoE (USA); STFC and UKSA (UK); CSIC, MINECO, JA, and RES (Spain); Tekes, AoF, and CSC (Finland); DLR and MPG (Germany); CSA (Canada); DTU Space (Denmark); SER/SSO (Switzerland); RCN (Norway); SFI (Ireland); FCT/MCTES (Portugal); and ERC and PRACE (EU). A description of the Planck Collaboration and a list of its members, indicating which technical or scientific activities they have been involved in, can be found at <http://www.cosmos.esa.int/web/planck/>. This work have been partially supported by INAF/Trieste Astronomical Observatory through “Ricerca di Base 2019” F.U. 1.05.01.01. M. M. acknowledges Maria Teresa Capria for useful suggestions about models of planetary atmospheres. The authors acknowledge the staff of the Library of the INAF/Trieste Astronomical Observatory: Laura Abrami and Chiara Doz, for their kind help in recovering the needed bibliography during the lockdown imposed in Italy by the COVID 19 pandemic. The authors thank the two anonymous referees for their suggestions, which helped to considerably improve the paper. This research made use of *Astropy*,¹⁴ a community-developed core Python package for astronomy (Astropy Collaboration et al. 2013; Price-Whelan et al. 2018); *EMCEE*¹⁵ (Foreman-Mackey et al. 2013) *HEALPix*¹⁶ (Górski et al.

¹⁴ <http://www.astropy.org>

¹⁵ <https://github.com/dfm/emcee>

¹⁶ <https://healpix.jpl.nasa.gov>

2005); HEALPy¹⁷ (Zonca et al. 2019); IPython¹⁸ (Pérez & Granger 2007); Matplotlib¹⁹ (Hunter 2007); NumPy²⁰ (Virtanen et al. 2020); Pandas²¹ (McKinney 2010). PyQuarantine²² SciPy²³ (Virtanen et al. 2020); WebPlotDigitizer²⁴ (McKinney 2010).

¹⁷ <https://github.com/healpy/healpy>

¹⁸ <https://ipython.org>

¹⁹ <https://matplotlib.org>

²⁰ <https://numpy.org>

²¹ <https://pandas.pydata.org>

²² <https://www.ict.inaf.it/gitlab/michele.maris/pyquarantine.git>

²³ <https://www.scipy.org>

²⁴ <https://automeris.io/WebPlotDigitize>

Table A.1: Range of variability^a for $\Delta T_{\text{ant,p}}$, in mK_{cmb} .

Planet	30 GHz	44 GHz	70 GHz
Jupiter	38.5 – 42.7	54.2 – 99.1	307.7 – 368.5
Saturn	6.1 – 7.0	8.2 – 1.6	45.5 – 55.6
Uranus	0.06 – 0.5	0.3 – 0.9	0.7 – 2.7
Neptune	0.02 – 0.3	0.04 – 0.5	0.06 – 1.3

^a Results represents the distribution over the whole set of transits and radiometers for each channel.

Appendix A: Technical aspects of the data analysis procedure

In this appendix, we provide more information about some of the most technical issues we have tackled to produce estimates for brightness temperatures.

Appendix A.1: Selection of samples and ROI

We have used the *Horizons* web service²⁵ to compute the apparent position of the planet for each sample in the time-ordered data acquired by the *Planck*/LFI radiometers. Using these positions, we have selected those samples within the stability period of each pointing period according to the following criteria: (a) they are not flagged as bad, (b) their pointing direction in the sky is within 5° from the planet (the Region-of-Interest, ROI). This radius limits the amount of data to process to a reasonable amount, and it permits to fully cover the angular size of the main beam; moreover, it is large enough to estimate the contribution of the background. The 5° angular size separates the intermediate beam region and the far sidelobe region, for which the *Planck* collaboration provides GRASP beam maps (Planck Collaboration 2016b).

We have divided the 5° radius ROI, in three concentric regions: the planet ROI is the ring with radius $R_{\text{ROI-I}} = 1.3$ FWHM of the beam, used to estimate $\Delta T_{\text{ant,p}}$; the avoidance ROI is the annulus between $R_{\text{ROI-I}}$ and $R_{\text{ROI-II}} = 2$ FWHM; finally, the background ROI is everything within $R_{\text{ROI-II}}$ and R_{ROI} . Typical values for $R_{\text{ROI-I}}$ are about $\approx 0.7^\circ$, $\approx 0.5^\circ$, $\approx 0.3^\circ$ at 30, 44, and 70 GHz respectively, while for $R_{\text{ROI-II}}$ $\approx 1.1^\circ$, $\approx 0.8^\circ$, $\approx 0.4^\circ$. The number of samples in the planet ROI is in the range $10^3 \div 10^4$; the number of samples in the background ROI is in the range of $10^5 \div 10^6$. Due to changes in the scanning strategy during the mission, the density of samples in the ROI largely changed among different transits.

As an example, Fig. 3 shows the classification and masking of data in the first transit, for radiometer LFI27-0 (30 GHz).

Appendix A.2: Background modelling

In Planck Collaboration (2014d, 2016c), the background was modelled as a constant derived from the median of the Background ROI. The constant included contributions from diffused foregrounds, CMB, point sources, and zero-point differences among different radiometers. However, after having masked point sources, the typical RMS of the diffuse background ($\Delta T_{\text{ant,p}}$) in the Background ROI is $\text{RMS}_{\text{background}} \approx 10^{-4} \text{K}_{\text{cmb}}$. Compared to $\Delta T_{\text{ant,p}}^*$ for the planets observed by *Planck*/LFI (Table A.1), it is evident that this fluctuation is equivalent to $\text{RMS}_{\text{background}}/\Delta T_{\text{ant,p}}^* \approx (0.6 \cdots 5) \times 10^{-3}$ of the Jupiter signal, which is negligible. For weaker planets, background fluctuations are more relevant: for Saturn $\text{RMS}_{\text{background}}/\Delta T_{\text{ant,p}}^* \approx (0.4 \div 3) \times 10^{-2}$, for Uranus $\text{RMS}_{\text{background}}/\Delta T_{\text{ant,p}}^* \approx 0.1 \div 0.6$, and for Neptune $\text{RMS}_{\text{background}}/\Delta T_{\text{ant,p}}^* \approx 0.2 \div 1.4$. Proper background removal is mandatory for all the planets but Jupiter.

To remove the background, we used the *Planck* 2018 sky maps to build a timeline $b_{k,t}$ for each transit and each radiometer. These timelines were computed using bilinear interpolation on the sphere at each pointing direction $\hat{\mathbf{P}}_t$. As for planets, we considered smearing too (see Sect. A.4). Since sky maps refer to the central frequency of the channel, the simulated timelines $b_{k,t}$ do not account for differences in bandpasses among different radiometers. To fix this, we introduced a scaling parameter α_{bck} and a zero point z_{bck} in the fit, so that $b_t = \alpha_{\text{bck}} b_{k,t} + z_{\text{bck}}$. We determined the parameters α_{bck} and z_{bck} for each radiometer by fitting the background model against the samples in the background ROI. Typical α_{bck} varies from 0.5 to 1.3, while z_{bck} varies within $\pm 0.2 \text{mK}_{\text{cmb}}$.

Fig. 3 in the top-right frame shows a background map derived from b_t . In the bottom-left frame, we show the histogram of the background model using green dots, and we overlap a Gaussian distribution with the same mean and RMS (red line). The long tail in the right wing of the distribution is due to the bright source on the lower-left corner of the map. We used a simple σ -clipping, whose threshold is shown as a dashed blue line in the plot, to mask that region (bottom-right part of the figure).

Appendix A.3: Bandpasses and beam patterns

Equation (22) shows that proper modelling of the beam shape is critical. The results presented here are based on the official band-averaged beam model, computed using GRASP. We derived a band-averaged map of the beam out of a set of gridded monochromatic maps, which were weighted according to the product between the SED of the incoming radiation and the bandpass of the radiometer. For planets, we used a ν^2 SED, as it represents the SED of a planet emitting in the Rayleigh-Jeans regime. To estimate $g_{p,t}^{(\text{ba})}$ (Sect. 2.3), we converted the instantaneous position of the planet in the (u_t, v_t) coordinates using Eq. (8), and we recovered the beam response using bilinear interpolation.

²⁵ <https://ssd.jpl.nasa.gov/?ephemerides>

There is a strong connection between the reduction of Jupiter observations and the estimation of the beam model, as the former requires the latter, but the latter is usually validated through the former. Unfortunately, carrying on the two analysis tasks at the same time is prohibitive, due to the computational time required by GRASP to estimate beam maps. Therefore, in our analysis we had to assume the correctness of the GRASP's beam models produced by the *Planck*/LFI collaboration.

Appendix A.4: Smearing

The signal acquired by *Planck*/LFI radiometers is integrated over a discrete sampling time, δt_{samp} , which depends on the frequency of the detector (30, 44, or 70 GHz) and is in the range 0.01–0.03 s. In that time, the planet moves across the beam and causes what is called *smearing*. Smearing causes the signal to be smoothed and must be properly taken in account in data analysis, because it tends to reduce the value of $\Delta T_{\text{ant,p}}^*$ (about 1.4% at 30 GHz, 1.1% at 44 GHz and 1.2% at 70 GHz). The amount of smearing is constant, as δt_{samp} for each radiometer is tuned to allow the beam to move by $\approx \text{FWHM}/3$.

To model the smearing effect, a common approach is to create a beam map by stacking and averaging a number of repetitions of the simulated GRASP beam map, shifted along the direction of scan by a fixed amount. However, this approach neglects the fact that the spin rate and the effective boresight angles can change during the mission. Therefore, we used a different strategy to deal with smearing: we over-sampled the modelled beam pattern along the path of the apparent motion of the planet in the beam reference frame, averaging the result.

To compute the planetary smearing for the i -th sample taken at time t_i , we took a triad of consecutive positions of the planet in the beam reference frame (u, v) at times t_{i-1} , t_i and t_{i+1} . Given that the u and v directions are orthogonal, the motion is described by the equations

$$u(l) \approx A_{u,i}l^2 + B_{u,i}l + C_{u,i}, \quad (\text{A.1})$$

$$v(l) \approx A_{v,i}l^2 + B_{v,i}l + C_{v,i}, \quad (\text{A.2})$$

with $l = (t - t_i)/\delta t_{\text{samp}}$, so that $l = -1, 0, +1$ respectively for samples $i - 1, i, i + 1$. We derived the coefficients $A_{u,i}$, $B_{u,i}$ and $C_{u,i}$ from the positions u_{i-1} , u_i and u_{i+1} using least squares minimization. The result is

$$A_{u,i} = \frac{u_{i+1} + u_{i-1}}{2} - u_i, \quad (\text{A.3})$$

$$B_{u,i} = \frac{u_{i+1} - u_{i-1}}{2}, \quad (\text{A.4})$$

$$C_{u,i} = u_i, \quad (\text{A.5})$$

and identical expressions can be derived for $A_{v,i}$, $B_{v,i}$, $C_{v,i}$ replacing u with v . We implemented over-sampling through an evaluation of the beam response over a number of positions N_{smear} calculated for $-\frac{1}{2} \leq l \leq +\frac{1}{2}$ and including the background. Our tests showed that $N_{\text{smear}} = 11$ is sufficient. We applied a similar procedure for the background calculation too, as mentioned in Sect. A.2.

Appendix A.5: Geometric corrections

Geometric corrections have to be introduced to correct for different conditions of observations, in particular differences in planet-observer distances and planet aspect angles²⁶. The WMAP collaboration reduced all the observations to a fiducial distance before computing T_b (Weiland et al. 2011; Bennett et al. 2013). While this step is not needed to recover T_b , as those effects can be directly accounted in the fit, it is convenient for the discussion to add it. A geometrical correction factor is defined as

$$f_{\text{geom}} = \frac{\tilde{\Omega}_p}{\Omega_p} \frac{1}{1 + f_{\text{asp}}}, \quad (\text{A.6})$$

where Ω_p is the planet solid angle at the epoch of observation, $\tilde{\Omega}_p$ is the planet solid angle at an arbitrary fiducial planet-planck distance, in our case the distance of the first transit. Planets are oblate spheroids, so that the solid angle depends on the latitude of the observer as seen from the Planet D_p (the sub-*Planck* point). Consequently, a fiducial Ω_p may refer to an observer looking at the pole or at the equator. The difference between the two conventions is 6.9% for Jupiter T_b , 10.9% for Saturn (only the disk), 2.3% for Uranus, and 1.7% for Neptune. Here we follow the convention in Weiland et al. (2011); Bennett et al. (2013); Planck Collaboration (2017), and we refer to observation at the equator²⁷. In this way

$$\Omega_p = \frac{\pi R_{\text{eq}} R_{\text{pol}}}{\Delta^2}, \quad (\text{A.7})$$

with Δ being the distance of the planet from *Planck* at the epoch of observation, and R_{eq} , R_{pol} the equatorial and the polar radius of the planet. In our observations, Ω_p are in the ranges $(2.7 \div 3.1) \times 10^{-8}$ sterad for Jupiter, $(4.8 \div 5.4) \times 10^{-9}$ sterad for Saturn, $(2.2 \div 2.3) \times 10^{-10}$ sterad for Uranus, and $(9.4 \div 9.6) \times 10^{-11}$ sterad for Neptune.

²⁶ Usually, analysis of planets assumes that a planet has a well-defined radius (i.e., the planet is a solid object). For a gas giant this is not true, since limb darkening and brightness temperature distribution across layers makes the radius a function of ν , so that different instruments with different bandpass sees different Ω_p . Analysis of this problem is postponed to another paper.

²⁷ In Planck Collaboration (2014d), the fiducial Ω_p was taken at the pole.

The term f_{asp} accounts for the fact that the planet is not always seen with the same aspect angle, i.e., the same *sub-Planck latitude* D_P :

$$1 + f_{\text{asp}} = \frac{\sqrt{(R_{\text{pol}} \cos D_P)^2 + (R_{\text{eq}} \sin D_P)^2}}{R_{\text{pol}}}. \quad (\text{A.8})$$

The correction is tiny, as f_{asp} is $2.1 \times 10^{-6} \div 3 \times 10^{-4}$ for Jupiter, $1.9 \times 10^{-4} \div 4.4 \times 10^{-3}$ for Uranus, and $3.7 \times 10^{-3} \div 4.1 \times 10^{-3}$ for Neptune. For Saturn, the disk would require a correction of the order $1.6 \times 10^{-4} \div 1.8 \times 10^{-2}$. However, having to account for the rings, we applied this correction together with the one required for the rings (see Sect. 4.2).

Appendix A.6: Aperture correction

Our fitting code assumes that every signal outside the $R_{\text{ROI-II}}$ is background. However, the beam extends outside $R_{\text{ROI-II}}$, so that the spilled signal is removed as background. The aperture correction is defined as

$$1 + f_{\text{aper}} = \frac{\int_{2\pi} d\varphi \int_0^\pi d\theta \sin \theta \gamma_p^{(\text{ba})}(\hat{\mathbf{P}})}{\int_{2\pi} d\varphi \int_0^{R_{\text{ROI-II}}} d\theta \sin \theta \gamma_p^{(\text{ba})}(\hat{\mathbf{P}})}. \quad (\text{A.9})$$

Typically, $f_{\text{aper}} \sim 10^{-3}$; they are listed in Table 1.

Appendix A.7: Beam model efficiency

The integral over 4π of an ideal beam model must be normalized to some reference value, which is usually either 1 or 4π . However, real models computed with GRASP suffers numerical errors giving a slightly smaller results than the reference value. These numerical errors have many origins; the most important are (1) the spatial resolution of the beam pattern, and (2) the order of the approximation used by GRASP to propagate the electromagnetic field through the telescope. The effect has a magnitude of some 10^{-3} and its value for each radiometer is reported in Table 1, column f_η . The quantity f_η is defined as

$$f_\eta = 1 - \int_{4\pi} d\Omega \gamma_{\text{GRASP},\nu}(\hat{\mathbf{P}})/4\pi. \quad (\text{A.10})$$

As this effect resembles a power loss in the beam, we dubbed f_η as *beam model efficiency*.

There are two possible corrections to this effect. Firstly, we could assume that the GRASP model is the correct beam model scaled by $1 - f_\eta$. In this case, $\Omega_{\text{beam}}^{(\text{ba})}$ is not affected by the beam model efficiency, but the measured $\Delta T_{\text{ant,p}}$ is scaled up by a systematic factor $1/(1 - f_\eta)$. This was the assumption used in Planck Collaboration (2016c). The problem with this approach is that the systematic effect leading to $f_\eta \neq 0$ is supposed to be equally distributed between the main beam and the sidelobes. However, a GRASP model is built to reproduce beam maps obtained from bright point sources, which are primarily sensitive to the shape of the main beam. Therefore, the cause for $f_\eta \neq 0$ is likely in the sidelobe pattern, which cannot be easily constrained by observations. Another possibility is that $g_t^{(\text{ba})}$ is unaffected by the problem, but the value of $\Omega_{\text{beam}}^{(\text{ba})}$ that has been derived from the model is erroneously scaled down by $1 - f_\eta$.

The truth is likely somewhere in the middle, and the measured brightness must be corrected by a an unknown factor $1 + x$, with $-f_\eta \leq x \leq +f_\eta$. As we could not tell what is the proper correction to apply, we avoided this step and left it as a source of uncertainty with a flat distribution in the range $[-f_\eta, f_\eta]$. Appendix A.12 provides more details of how this is accounted in Monte Carlo simulations and bootstrap analyses.

Being a systematic effect, this error should be quoted separately as an unknown scaling factor applied to $T_{\text{b,rj}}$, $T_{\text{b,c}}$, or $T_{\text{b}}^{(\text{ba})}$. However, if we are estimating a total uncertainty budget, it is possible to consider it as a random value with variance $f_\eta^2/3$, which can be added to the noise variance. This is clear in the analysis of $T_{\text{b,rj}}$, $T_{\text{b,c}}$ or $T_{\text{b}}^{(\text{ba})}$ derived from Monte Carlo simulations and bootstrap methods. A more conservative approach would be to drop the $1/3$ factor and simply add f_η^2 to the variance.

Appendix A.8: Sidelobes

It is customary to include only the main beam in the value of Ω_{beam} . Correction for the power spilled in the sidelobes is usually accounted with a term $1 + f_{\text{SL}}$ that corrects for the sidelobes efficiency (Planck Collaboration 2014d, 2016c). In this work, we do not follow this convention as we integrated $\Omega_{\text{beam}}^{(\text{ba})}$ over the whole 4π sphere; therefore, no f_{SL} correction is needed.

Appendix A.9: Blocking

Blocking can be considered as a negative contribution to brightness, as in Eq. (26), or as a correction on the brightness temperature. The former quantity is listed in Table 1, in Table A.2 we provide the corresponding antenna temperatures.

Table A.2: Blocking corrections as antenna temperatures.

Planet	$\Delta T_{\text{ant,block}} [\text{K}_{\text{cmb}}]$		
	30 GHz	44 GHz	70 GHz
Jupiter	6.0×10^{-4}	8.0×10^{-4}	3.0×10^{-3}
Saturn	1.1×10^{-4}	1.4×10^{-4}	4.9×10^{-4}
Uranus	4.8×10^{-6}	6.2×10^{-6}	2.2×10^{-5}
Neptune	2.0×10^{-6}	2.6×10^{-6}	9.2×10^{-6}

Appendix A.10: $\left(\frac{dB_\nu}{dT}\right)_{\text{cmb}}$

The $\left(\frac{dB_\nu}{dT}\right)_{\text{cmb}}$ factor is used to convert the antenna temperature $\Delta T_{\text{ant,p}}$ into a brightness, like in Eq. (21). The assumption that the CMB spectrum follows the Rayleigh-Jeans law ($\left(\frac{dB_\nu}{dT}\right)_{\text{cmb}} \propto \nu^2$), leads to overestimate the brightness of $\approx 12\%$ at 70 GHz, of 5% at 44 GHz and 2.2% at 30 GHz. Replacing $\left(\frac{dB_\nu}{dT}\right)_{\text{cmb}}^{(\text{ba})}$ with $\left(\frac{dB_\nu}{dT}\right)_{\text{cmb}}$ has the effect of slightly underestimate the brightness of $4.5 \times 10^{-3} \dots 6.9 \times 10^{-3}$ at 30 GHz, $2.1 \times 10^{-3} \dots 3.2 \times 10^{-3}$ at 44 GHz and $1.7 \times 10^{-3} \dots 3.6 \times 10^{-3}$ at 70 GHz.

Appendix A.11: Band averaged B_ν

To solve for $T_{\text{b}}^{(\text{ba})}$ from Eq. (29), we exploit the fact that $B_\nu^{(\text{ba})}(T_{\text{b}})$ is a nearly-linear increasing function of T_{b} . For each radiometer, we tabulate the quantity

$$B_\nu^{(\text{ba})}(T_{\text{b}}) = \frac{1}{\Delta\nu} \int_0^{+\infty} d\nu \tau(\nu) B_\nu(\nu, T_{\text{b}}); \quad (\text{A.11})$$

for $10 \text{ K} \leq T_{\text{b}} \leq 500 \text{ K}$ in steps of 1 K. The tabulated function is then inverted by interpolating T_{b} as a function of measured B_{p} , using the right side of Eq. (29) as input.

It is interesting to compare the difference in T_{b} accounting for band averaging versus simple analytical inversion of $B_{\text{p}} = B_\nu(\nu_{\text{cent}}, T_{\text{b}})$. For this, we can define a further correction factor $1 + f_{\text{TbBa}} = T_{\text{b}}^{(\text{ba})}/B_\nu^{-1}(\nu_{\text{cent}}, B_{\text{p}})$. In all the cases, $f_{\text{TbBa}} < 0$: this means that neglecting band averaging causes an overestimation of T_{b} . The quantity f_{TbBa} varies in the range 3.9×10^{-3} to 8.2×10^{-3} , depending on the radiometer. Differences in brightness temperatures are in the range -1.5 K to -0.5 K , depending on the radiometer and the planet. Different planets and/or transits alters f_{TbBa} by less than 10^{-5} .

Appendix A.12: Averaged values

There are various ways to compute averaged values from our list of measurements B_{p} , $T_{\text{b,rj}}$, $T_{\text{b,c}}$ and $T_{\text{b}}^{(\text{ba})}$ for a planet from each transit and radiometer.

The simplest method is to compose a subset of measurements specifying a list of transits and radiometers belonging to a given frequency channel and then to derive the weighted average of B_{p} , $T_{\text{b,rj}}$, $T_{\text{b,c}}$, and $T_{\text{b}}^{(\text{ba})}$. This is the approach used in Planck Collaboration (2016c), where channel averages were computed and then averaged across the transits. The final uncertainty $\sigma_{\bar{x}}$ of \bar{x} can be derived analytically using error propagation; however, if the distribution of x is not Gaussian, then unreasonably small $\sigma_{\bar{x}}$ are obtained.

A better approach is to follow a least-squares minimization, fitting \bar{x} to the list of x_i in the subset

$$\chi^2(\bar{x}) = \sum_i \frac{(\bar{x} - x_i)^2}{\sigma_i^2}, \quad (\text{A.12})$$

where x is either B_{p} , $T_{\text{b,rj}}$, $T_{\text{b,c}}$, or $T_{\text{b}}^{(\text{ba})}$, and σ_i is the uncertainty. As it is well known, the minimization of χ^2 gives the weighted average formula, but the use of numerical minimization codes, such as the `curve_fit` function in the SciPy package (Virtanen et al. 2020), can estimate $\sigma_{\bar{x}}$ from the covariance matrix of errors of fitted parameters, leading to a more prudent estimate of the uncertainty.

Alternatively, a bootstrap of fitting residuals $r_i = (x_i - \bar{x})/\sigma_i$ can be used to resample the input x_i , and to derive a distribution of possible values of \bar{x} from which $\sigma_{\bar{x}}$ can be obtained. Here we used the bootstrap algorithm provided by the `scikit-learn` package (Pedregosa et al. 2011).

Finally by defining a likelihood for \bar{x} : $\log P(\bar{x}|x_i) \propto -\chi^2(\bar{x})/2$ and a prior for \bar{x} , a posterior probability for \bar{x} can be formed and maximized. Uncertainties can be estimated with Monte Carlo simulations.

In this paper we follow all of those approaches to define the uncertainties of our estimated averaged values, employing `emcee` (Foreman-Mackey et al. 2013) for the estimation of uncertainties using Monte Carlo simulations. In general the results of the three methods are consistent each other, but in some cases the bootstrap approach provided larger uncertainties. We have chosen to take the largest uncertainty provided by the three methods for each averaged quantity.

Since $T_{b,c}$ and $T_b^{(ba)}$ are not additive quantities like B_p and $T_{b,rj}$, we have estimated $T_b^{(ba)}$ through the minimization of the quantity $\chi^2(T_b^{(ba)})$, defined as

$$\chi^2(T_b^{(ba)}) = \sum_i \frac{(B_{v,i}^{(ba)}(T_b^{(ba)}) - B_{p,i})^2}{\sigma_i^2}, \quad (\text{A.13})$$

where σ_i is the uncertainty on the measured $B_{p,i}$, and $B_{v,i}^{(ba)}(T)$ is the Black Body emissivity averaged over the bandpass for the radiometer that acquired the i -th sample.

The application of the bootstrap method requires to sample the residuals $r_i = (B_{v,i}^{(ba)}(T_b^{(ba)}) - B_{p,i})/\sigma_i$.

The application of the MCMC method requires to define the likelihood

$$\log P(B^{(ba)}|T_b^{(ba)}) = -\frac{1}{2} \sum_i \frac{(B_{v,i}^{(ba)}(T_b^{(ba)}) - B_{p,i})^2}{\sigma_i^2} - \sum_i \frac{1}{2} \log 2\pi\sigma_i^2, \quad (\text{A.14})$$

as well as the prior

$$\log P(T_b^{(ba)}) = \begin{cases} -\infty, & \text{if } T_b^{(ba)} \leq 0 \\ 0, & \text{if } T_b^{(ba)} > 0 \end{cases}, \quad (\text{A.15})$$

which constrains $T_b^{(ba)} > 0$. Similar formulas can be derived for $T_{b,c}$ by replacing $B_{v,i}^{(ba)}(T)$ with $B_v(\nu_{\text{cent},i}, T)$, where $\nu_{\text{cent},i}$ is the central frequency of sample i .

To investigate the effect of the uncertainty in the correction for the beam numerical efficiency described in Sect. A.7, we redefined the bootstrapped simulated brightness for sample i as

$$B_{\text{bstp},i}^{(ba)} = (1 - z_i f_{\eta,i})(B_{v,i}^{(ba)}(T_b^{(ba)}) + \rho_i), \quad (\text{A.16})$$

where $\{\rho_i\}$ is a list of residuals sampled from the distribution of $\{r_i\}$, $\{z_i\}$ is a list of random numbers taken from the uniform distribution $[-1, 1]$. Similarly, to investigate this effect using a Monte Carlo simulation we modified the likelihood in Eq. (A.14) by replacing $B_{v,i}^{(ba)}(T_b^{(ba)})$ with $B_{v,i}^{(ba)}(T_b^{(ba)})/(1 - z_i f_{\eta,i})$, where $\{z_i\}$ is a set of parameters with a flat distribution

$$\log P(z_i) = \sum_i \begin{cases} 0, & \text{if } -1 \leq z_i \leq 1; \\ -\infty, & \text{otherwise} \end{cases}, \quad (\text{A.17})$$

which multiplies the prior distribution for $T_b^{(ba)}$.

Since we are dealing with averaged quantities, we had to define a reference frequency. For each subset of measurements we took the weighted average of the ν_{cent} of each measure, using the σ_i as weights. As the relative errors for B_p , $T_{b,rj}$, $T_{b,c}$ and $T_b^{(ba)}$ are similar, the resulting averaged ν_{cent} is nearly independent on the choice of the quantity to be averaged.

Appendix A.13: Conversion of $T_{b,rj}^{(\text{wmap})}$ to T_b

WMAP provided planets brightness temperatures in form of $T_{b,rj}$ and without any correction for blocking (Weiland et al. 2011, ex.). To properly compare WMAP results to models, $T_{b,rj}$ must be converted either to $T_{b,c}$ or $T_b^{(ba)}$. In addition we must take in account the different value of the dipole amplitude used by *Planck* and WMAP, as this leads to a mismatch in the absolute calibration level. The *Planck* team used the value $A_{\text{Planck}} = 3364 \pm 2 \mu\text{K}$ (Planck Collaboration 2014d, 2016c, 2018b), while the WMAP team used $A_{\text{WMAP}} = 3355 \pm 8 \mu\text{K}$ (Hinshaw et al. 2009). Therefore, we scaled WMAP's estimates of $T_{b,rj}$ by a factor $G_{\text{WMAP,Planck}} = 1.002831 \pm 0.00246$.

For $T_{b,c}$ we solved for

$$B_v(\nu_{\text{cent}}, T_{b,c}) = (T_{b,rj} G_{\text{WMAP,Planck}} + \Delta T_{\text{ant,block}}) B_{v,rj,1}(\nu_{\text{cent}}), \quad (\text{A.18})$$

where $\Delta T_{\text{ant,block}}$ is provided by (Page et al. 2003) for the bands K, Ka, Q, V, and W assuming values 2.2, 2, 1.9, 1.5 and 1.1 K respectively. Note that both $B_{v,rj,1}(\nu)$ and $B_v(\nu, T)$ depend on frequency; we evaluated them at the central frequencies of each band as defined in Table 3 of Weiland et al. (2011).

For $T_b^{(ba)}$, we follow what we explained in Sect. A.11 and solve for

$$\frac{1}{\Delta\nu} \int_0^{+\infty} d\nu \tau(\nu) B_v(\nu, T_b^{(ba)}) = B_{v,rj,1}(\nu_{\text{cent}}) (T_{b,rj} G_{\text{WMAP,Planck}} + \Delta T_{\text{ant,block}}), \quad (\text{A.19})$$

where the bandpass $\tau(\nu)$ for each band is taken from the Lambda website²⁸.

²⁸ https://lambda.gsfc.nasa.gov/product/map/dr5/bandpass_info.cfm

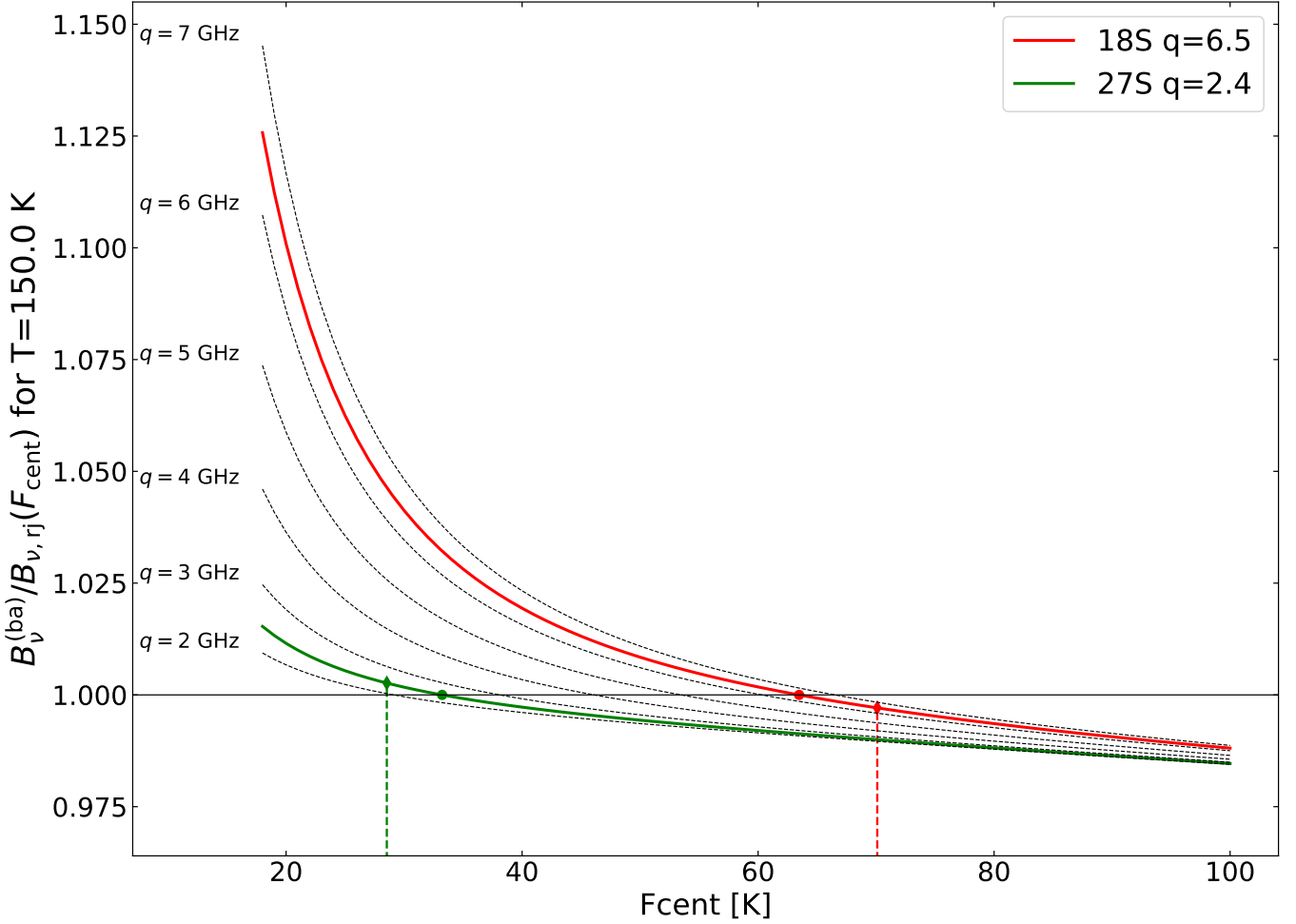


Fig. A.1: Plot of the ratio $B_{\nu}^{(\text{ba})}/B_{\nu,rj}(F_{\text{cent}})$ computed for $T = 150$ K as a function of ν_{cent} for the bandpasses of the radiometers 18S (thick red line) and 27S (thick green line), offseted in frequency, and for a set of top-hat bandpasses of different width (black thin lines). The vertical dashed lines indicates the central frequencies of the radiometers. The bandwidth of the bandpasses are expressed as function of the effective bandwidth q defined in Eq. (A.21). The q -values for the top-hat bandpasses are printed at the left of each curve, while the *Planck*/LFI bandpass is 6.5 GHz for 18S and 2.4 GHz for 27S..

We note that other authors like Gibson et al. (2005); Karim et al. (2018) convert $T_{b,rj}$ to $T_{b,c}$ applying an additive correction defined as follows:

$$T_{b,c} \approx T_{b,rj} + \Delta T_{\text{ant,block}} + \Delta T_{rj \rightarrow b}, \quad (\text{A.20})$$

with $\Delta T_{rj \rightarrow b}$ equal to 0.54, 0.79, 0.98, 1.46 and 2.23 K for the bands from K to W; this is because of the assumption that $B_{\nu}^{-1}(\nu, T) - T$ shows only a slight dependence on T for $\nu < 100$ GHz and $T > 100$ K. Here however we prefer to apply Eq. (A.13).

Finally, we want to underline the fact that the concise descriptions usually reported in the literature for this conversion leave some ambiguity in reproducing the published results. An example is Table 2 from Gibson et al. (2005). The authors quoted Page et al. (2003) and reported the value $T_{b,rj} = 146.6$ K, but after the application of several corrections they end with a new estimate $T_{b,rj} = 147.8$ K that is converted in their final $T_b^{\text{new}} = 148.4$ K by adding 0.79 K. However, the 0.79 K correction is the difference $T_{b,c,(Ka)}(148.4 \text{ K}) - 148.4 \text{ K}$ that is derived from Eq. (A.18), and not the difference $T_b^{(\text{ba})}(148.4 \text{ K}) - 148.4 \text{ K}$ from Eq. (A.19), which is 0.23 K. The authors state that they converted $T_{b,rj}$ to T_b through the integration of a black body ideal brightness over the WMAP bandpass. The difference is negligible when compared to the final uncertainties, so that the conclusions in Gibson et al. (2005); Karim et al. (2018) (as well as other papers that apply the same procedure) are not affected at all. But without the possibility to reconstruct their conversion procedure, it is difficult to judge whether small differences between our results and their results are significant or not.

Appendix A.14: $T_b^{(\text{ba})}$ and $T_{b,rj}$ relations

It might sound surprising that $T_{b,rj} < T_b^{(\text{ba})}$ for 70 GHz and 44 GHz data, while $T_{b,rj} > T_b^{(\text{ba})}$ for 30 GHz data. However, this is expected and is mainly a consequence of the interplay of bandwidth and Planck's law.

Table A.3: Effective bandwidth q and critical central frequency $\nu_{\text{cent},1}$.

	q [GHz]	$\nu_{\text{cent},1}$ ^a [GHz]		q [GHz]	$\nu_{\text{cent},1}$ [GHz]
18M	6.01	60.4	24M	2.54	34.2
18S	6.48	63.5	24S	2.76	36.0
19M	4.94	53.0	25M	2.53	34.0
19S	5.15	54.5	25S	2.43	33.2
20M	5.18	54.7	26M	2.88	37.1
20S	5.42	56.4	26S	2.31	32.0
21M	5.74	58.6	27M	2.01	29.2
21S	5.59	57.6	27S	2.44	33.2
22M	5.46	56.6	28M	2.21	31.2
22S	5.76	58.7	28S	2.47	33.5
23M	4.52	50.0			
23S	4.98	53.4			

^a $\nu_{\text{cent},1}$ is computed numerically at the reference value $T = 150$ K.

Let's assume that we are observing a source with brightness \mathcal{S} . Then, $T_{\text{b,rj}}$, $T_{\text{b,c}}$, and $T_{\text{b}}^{(\text{ba})}$ are solutions of the equations $\mathcal{S} = \mathcal{B}_{\nu,\text{rj}}(\mathcal{T}_{\text{b,rj}}, \nu_{\text{cent}})$ and $\mathcal{S} = \mathcal{B}_{\nu}^{(\text{ba})}(\mathcal{T}_{\text{b}}^{(\text{ba})})$. Given some temperature T , if $B_{\nu,\text{rj}}(T, \nu_{\text{cent}}) > B_{\nu}^{(\text{ba})}(T)$ then $T_{\text{b,rj}}(\mathcal{S}) < T_{\text{b}}^{(\text{ba})}(\mathcal{S})$, and vice versa.

We model bandpasses as top-hat functions with $\tau(\nu) = 1$ in the frequency range $\nu_{\text{cent}} - \delta/2 \leq \nu \leq \nu_{\text{cent}} + \delta/2$ and zero otherwise. However, to better model the nuances of *Planck*/LFI's bandpasses, instead of using Δ to characterize the bandwidth, we use the parameter q , defined as follows:

$$q = \sqrt{\frac{\int d\nu \tau(\nu) (\nu - \nu_{\text{cent}})^2}{\int d\nu \tau(\nu)}}, \quad (\text{A.21})$$

which reduces to $q = \delta/\sqrt{12}$ for a top-hat bandpass. With those conventions, whenever the RJ approximation and Planck's law agree, it follows that

$$B_{\nu}^{(\text{ba})}(T) \approx \frac{2k_{\text{b}}T\nu_{\text{cent}}^2}{c^2} \left(1 + \left(\frac{q}{\nu_{\text{cent}}} \right)^2 \right). \quad (\text{A.22})$$

Given that the bandpass is symmetrical and receives more contribution from the high-frequency side, the band-averaged brightness is larger than the monochromatic RJ. Consequently, in this approximation $T_{\text{b}}^{(\text{ba})} < T_{\text{b,rj}}$.

However as ν_{cent} increases, the RJ approximation overestimates the true black-body brightness. Because of this, above some central frequency $\nu_{\text{cent},1}$ we must have $B_{\nu}^{(\text{ba})} < B_{\nu,\text{rj}}$ and $T_{\text{b}}^{(\text{ba})} > T_{\text{b,rj}}$. The derivation of an approximated expression for $\nu_{\text{cent},1}$ is based on the factorization of Planck's law as the product of the RJ law and a dumping factor $x/(e^x - 1)$ with $x = h\nu/k_{\text{b}}T$. Given that we are in the limits of small x with a much smaller δ we may assume that over the bandpass $x/(e^x - 1) \approx x_c/(e^{x_c} - 1) \approx 1/(1 + x_c/2)$, with $x_c = h\nu_{\text{cent}}/k_{\text{b}}T$. Therefore, the band averaged brightness has again the form of the right side of Eq. (A.22), but scaled by the factor $x/(e^x - 1)$. The critical frequency is such that $B_{\nu}^{(\text{ba})}(T, \nu_{\text{cent},1})/B_{\nu,\text{rj}}(\nu_{\text{cent},1}) = 1$, and therefore

$$\nu_{\text{cent},1} \approx \sqrt[3]{\frac{2k_{\text{b}}T}{h}} q^{2/3}, \quad (\text{A.23})$$

if T is expressed in K and q in GHz, then $\nu_{\text{cent},1} \approx 3.47 T^{1/3} q^{2/3}$ GHz.

A representative case for *Planck*/LFI observations of Jupiter is $T = 150$ K and q in the range 1 GHz–6.5 GHz, resulting in $\nu_{\text{cent},1}$ in the range 18 GHz–64 GHz.

A more accurate calculation can be easily obtained numerically, and it is shown in Fig. A.1, where the ratio $B_{\nu}^{(\text{ba})}/B_{\nu,\text{rj}}(\nu_{\text{cent}})$ is calculated for the representative case $T = 150$ K. As expected from our calculation, since the dumping factor decreases with ν_{cent} , the ratio between the band-averaged brightness and the RJ brightness decreases too; the main parameter describing the curve is q . For radiometer 27S, $q \approx 2.4$ GHz: in fact, the corresponding line fits nicely between the top-hat bandpasses with $q = 2$ GHz and $q = 3$ GHz. We find a similar behavior for 18S, with $q \approx 6.5$ GHz.

For the *Planck*/LFI radiometers, $\nu_{\text{cent},1}$ always falls within the range 29.1 GHz–66.5 GHz. In particular:

- For 27S, we derive numerically $\nu_{\text{cent},1} = 29.2$ GHz, while the analytical approximation gives 30 GHz;
- For 18S, we derive 63.5 GHz and 64 GHz, for the numerical case and the analytical approximation respectively.

The explanation of the inverted behaviour of $T_b^{(ba)}$ and $T_{b,rj}$ at 30 GHz and at 70 GHz is now clear. For 27S, $\nu_{\text{cent}} = 28.5$ GHz, just below its critical value, so for this channel $B_v^{(ba)} > B_{v,rj}(\nu_{\text{cent}})$ and $T_b^{(ba)} < T_{b,rj}$. On the contrary, for 18S $\nu_{\text{cent}} = 70.1$ GHz, slightly above its critical value: this results in $B_v^{(ba)} < B_{v,rj}(\nu_{\text{cent}})$ and $T_b^{(ba)} > T_{b,rj}$. Last but not least, the 44 GHz radiometers have q comparable to those of the 30 GHz, since $\nu_{\text{cent},1} \approx 30$ GHz, smaller than their central frequencies: therefore, they behave as the 70 GHz radiometers.

Table A.3 provides the estimates for q and $\nu_{\text{cent},1}$ for all the *Planck*/LFI radiometers. We computed the values for $\nu_{\text{cent},1}$ by numerical integration at the reference temperature of 150 K. These values can be scaled to different temperatures in the range 125 K–175 K by using the $\sqrt[3]{T}$ dependence of Eq. (A.23) within a two percent accuracy.

References

- Astropy Collaboration, Robitaille, T. P., Tollerud, E. J., et al. 2013, *A&A*, 558, A33
- Ben-Reuven, A. 1966, *Physical Review*, 145, 7
- Bendo, G. J., Griffin, M. J., Bock, J. J., et al. 2013, *MNRAS*, 433, 3062
- Bennett, C. L., Larson, D., Weiland, J. L., et al. 2013, *ApJS*, 208, 20
- Bertinocourt, B., Lagache, G., Martin, P. G., et al. 2016, *A&A*, 588, A107
- Cunningham, C. T., Ade, P. A. R., Robson, E. I., Nolt, I. G., & Radostiz, J. V. 1981, *Icarus*, 48, 127
- de Pater, I. 1981, *A&A*, 93, 370
- de Pater, I. 2018, *Nature Astronomy*, 2, 364
- de Pater, I., Butler, B., Sault, R. J., et al. 2018, in *Astronomical Society of the Pacific Conference Series*, Vol. 517, *Science with a Next Generation Very Large Array*, ed. E. Murphy, 49
- de Pater, I. & Dickel, J. R. 1991, *Icarus*, 94, 474
- de Pater, I. & Dunn, D. E. 2003, *Icarus*, 163, 449
- de Pater, I., Fletcher, L. N., Luszcz-Cook, S., et al. 2014, *Icarus*, 237, 211
- de Pater, I., Heiles, C., Wong, M., et al. 1995, *Highlights of Astronomy*, 10, 637
- de Pater, I., Kenderdine, S., & Dickel, J. R. 1982, *Icarus*, 51, 25
- de Pater, I. & Massie, S. T. 1985, *Icarus*, 62, 143
- de Pater, I. & Mitchell, D. L. 1993, *J. Geophys. Res.*, 98, 5471
- de Pater, I. & Richmond, M. 1989, *Icarus*, 80, 1
- de Pater, I., Romani, P. N., & Atreya, S. K. 1991, *Icarus*, 91, 220
- de Pater, I., Sault, R. J., Butler, B., DeBoer, D., & Wong, M. H. 2016, *Science*, 352, 1198
- de Pater, I., Sault, R. J., Moeckel, C., et al. 2019a, *AJ*, 158, 139
- de Pater, I., Sault, R. J., Wong, M. H., et al. 2019b, *Icarus*, 322, 168
- Dunn, D. E., de Pater, I., & Sault, R. J. 2003, *Icarus*, 165, 121
- Dunn, D. E., de Pater, I., Wright, M., Hogerheijde, M. R., & Molnar, L. A. 2005, *AJ*, 129, 1109
- Dunn, D. E., Molnar, L. A., & Fix, J. D. 2002, *Icarus*, 160, 132
- Encrenaz, T. & Moreno, R. 2002, in *American Institute of Physics Conference Series*, Vol. 616, *Experimental Cosmology at Millimetre Wavelengths*, ed. M. de Petris & M. Gervasi, 330–337
- Epstein, E. E., Janssen, M. A., Cuzzi, J. N., Fogarty, W. G., & Mottmann, J. 1980, *Icarus*, 41, 103
- Foreman-Mackey, D., Hogg, D. W., Lang, D., & Goodman, J. 2013, *PASP*, 125, 306
- Gibson, J., Welch, W. J., & de Pater, I. 2005, *Icarus*, 173, 439
- Goldin, A. B., Kowitt, M. S., Cheng, E. S., et al. 1997, *ApJ*, 488, L161
- Górski, K. M., Hivon, E., Banday, A. J., et al. 2005, *ApJ*, 622, 759
- Greve, A., Steppe, H., Graham, D., & Schalinski, C. J. 1994, *A&A*, 286, 654
- Griffin, M. J., North, C. E., Schulz, B., et al. 2013, *MNRAS*, 434, 992
- Griffin, M. J. & Orton, G. S. 1993, *Icarus*, 105, 537
- Grossman, A. W., Muhleman, D. O., & Berge, G. L. 1989, *Science*, 245, 1211
- Gulkis, S., Janssen, M. A., & Olsen, E. T. 1978, *Icarus*, 34, 10
- Hazumi, M., Ade, P. A. R., Akiba, Y., et al. 2019, *Journal of Low Temperature Physics*, 194, 443
- Hinshaw, G., Weiland, J. L., Hill, R. S., et al. 2009, *ApJS*, 180, 225
- Hunter, J. D. 2007, *Computing in Science and Engineering*, 9, 90
- Janssen, M. A., Ingersoll, A. P., Allison, M. D., et al. 2013, *Icarus*, 226, 522
- Janssen, M. A. & Olsen, E. T. 1978, *Icarus*, 33, 263
- Joiner, J. & Steffes, P. G. 1991, *J. Geophys. Res.*, 96, 17,463
- Karim, R. L., DeBoer, D., de Pater, I., & Keating, G. K. 2018, *AJ*, 155, 129
- Keihänen, E., Kurki-Suonio, H., Poutanen, T., Maino, D., & Burigana, C. 2004, *A&A*, 428, 287
- Klein, M. J., Bolton, S. J., Gulkis, S., et al. 2001, in *Planetary Radio Emissions V*, 221–228
- Klein, M. J. & Gulkis, S. 1978, *Icarus*, 35, 44
- Klein, M. J. & Hofstadter, M. D. 2006, *Icarus*, 184, 170
- Klein, M. J., Janssen, M. A., Gulkis, S., & Olsen, E. T. 1978, in *NASA Conference Publication*, Vol. 2068, *NASA Conference Publication*, 195–216
- Kloosterman, J. L., Dunn, D. E., & de Pater, I. 2005, *ApJS*, 161, 520
- Kramer, C., Moreno, R., & Greve, A. 2008a, *A&A*, 482, 359
- Kramer, C., Moreno, R., & Greve, A. 2008b, *A&A*, 482, 359
- Lellouch, E. & Destombes, J. L. 1985, *A&A*, 152, 405
- Maino, D., Burigana, C., Górski, K. M., Mandolesi, N., & Bersanelli, M. 2002, *A&A*, 387, 356
- Maris, M. & Burigana, C. 2009, *Earth Moon and Planets*, 105, 81
- McKinney, W. 2010, in *Proceedings of the 9th Python in Science Conference*, ed. S. van der Walt & J. Millman, 51 – 56
- Mennella, A., Bersanelli, M., Butler, R. C., et al. 2010, *A&A*, 520, A5+
- Moreno, R. 1998, PhD thesis, UNIVERSITE PARIS VI, thèse de doctorat dirigée par Marten, André Terre, océan, espace Paris 6 1998, 1998PA066248
- Muhleman, D. O. & Berge, G. L. 1991, *Icarus*, 92, 263
- Müller, T. G., Balog, Z., Nielbock, M., et al. 2016, *A&A*, 588, A109
- Orton, G. S., Fletcher, L. N., Moses, J. I., et al. 2014, *Icarus*, 243, 494
- Page, L., Barnes, C., Hinshaw, G., et al. 2003, *ApJS*, 148, 39
- Pedregosa, F., Varoquaux, G., Gramfort, A., et al. 2011, *Journal of Machine Learning Research*, 12, 2825
- Pérez, F. & Granger, B. E. 2007, *Computing in Science and Engineering*, 9, 21
- Planck Collaboration. 2014a, *A&A*, 571, A1
- Planck Collaboration. 2014b, *A&A*, 571, A3

- Planck Collaboration. 2014c, *A&A*, 571, A4
Planck Collaboration. 2014d, *A&A*, 571, A5
Planck Collaboration. 2016a, *A&A*, 594, A3
Planck Collaboration. 2016b, *A&A*, 594, A4
Planck Collaboration. 2016c, *A&A*, 594, A5
Planck Collaboration. 2017, *A&A*, 607, A122
Planck Collaboration. 2018a, arXiv e-prints, arXiv:1807.06205
Planck Collaboration. 2018b, arXiv e-prints, arXiv:1807.06206
Price-Whelan, A. M., Sipőcz, B. M., Günther, H. M., et al. 2018, *AJ*, 156, 123
Santos-Costa, D., Bolton, S. J., Sault, R. J., Thorne, R. M., & Levin, S. M. 2011, *Journal of Geophysical Research (Space Physics)*, 116, A12236
Schloerb, F. P., Muhleman, D. O., & Berge, G. L. 1979a, *Icarus*, 39, 232
Schloerb, F. P., Muhleman, D. O., & Berge, G. L. 1979b, *Icarus*, 39, 214
Teyssier, D. & Marston, A. 2017, Release notes: Herschel Planetary Calibrator models, Tech. Rep. 1-0, ESA
The BeyondPlanck Collaboration. 2020, BeyondPlanck I. Global Bayesian analysis of the Planck Low Frequency Instrument data
Tollefson, J., de Pater, I., Luszcz-Cook, S., & DeBoer, D. 2019, *AJ*, 157, 251
van der Tak, F., de Pater, I., Silva, A., & Millan, R. 1999, *Icarus*, 142, 125
Virtanen, P., Gommers, R., Oliphant, T. E., et al. 2020, *Nature Methods*
Weiland, J. L., Odegard, N., Hill, R. S., et al. 2011, *APJS*, 192, 19
Zonca, A., Singer, L., Lenz, D., et al. 2019, *The Journal of Open Source Software*, 4, 1298